Engineering Structures 323 (2025) 119220

Contents lists available at ScienceDirect

Engineering Structures

journal homepage: www.elsevier.com/locate/engstruct

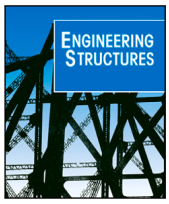

A novel approach to model differential settlements and crack patterns in masonry structures

Antonino Iannuzzo [a], Vincenzo Mallardo [b,*]

[a] Department of Engineering, University of Sannio Piazza Roma 21, Benevento, 82100, Italy
[b] Department of Architecture, University of Ferrara via Quartieri 8, Ferrara, 44121, Italy

ARTICLE INFO

Keywords:
Historical structures
Integral equation
BEM
Energy formulation
Contact analysis
Iterative approach
Dry masonry
Rigid block model
No-tension material

ABSTRACT

The present paper introduces a novel methodology for accurately modelling differential settlements beneath the foundations of masonry structures and the resulting crack patterns. In contrast to standard strategies, which typically impose predefined settlements at the structure's base, the proposed approach directly accounts for the soil–structure interaction by coupling the mechanical responses of masonry and soil. Specifically, the mechanical behaviour of the masonry is accurately modelled using an elastic no-tension approach, while the soil is represented as an elastic half-plane. The solution to the coupled mechanical problem, satisfying both equilibrium and compatibility conditions, is obtained through an iterative optimisation-based procedure. Several 2D numerical applications, considering different geometries and loading conditions, are provided to demonstrate the proposed procedure's effectiveness and performance and highlight its potential.

1. Introduction

Masonry buildings constitute a significant portion of the historical centres in Europe and Asia. Nowadays, these structures serve as popular tourist attractions and as housing for public establishments such as museums, offices, galleries, and private facilities, including apartments, charitable organisations, and shops. Therefore, it is essential to assess their structural vulnerability to provide correct and reliable information to the population, stakeholders, administrations, and other relevant parties, thus enabling informed decision-making while ensuring the safety and preservation of these valuable assets.

One noticeable phenomenon commonly observed in ancient masonry structures is the occurrence of differential settlements. They pose a significant risk to the integrity of overhead masonry structures, leading to potential damages. Furthermore, they can compromise the structural integrity of the building, thereby reducing its seismic resilience.

Many scientific contributions (see, for instance, [1–14], and references therein) have focused their attention at identifying the most suitable theoretical and numerical models to predict the actual behaviour, considering both in- and out-of-plane problems. A recent review of such models is provided in [15]. For instance, in [11], the collapse mechanism induced by instability phenomena on masonry walls is investigated by 2D Finite Element (FE) approaches. A 2D model, arising from an enhanced kinematic approach for the nonlinear analysis of masonry walls subjected to in-plane loading conditions, is introduced in [7]. Similar accurate approaches involve fracture and damage-plastic or other nonlinear mechanisms in bricks and mortar [8,12] as well as homogenisation techniques [4]. Limit analysis computations have also been carried out to investigate the out-of-plane behaviour of masonry walls [16] with particular attention to curved horizontal masonry structures [17], in combination with homogenisation techniques [18], under dynamic action by the discrete element modelling [19], and by applying the Boundary Element Method (BEM) [20,21]. The Finite/Discrete Element Method (FDEM is another suitable approach that models problems involving static and dynamic behaviour of systems with a large number of solid deformable bodies such as bricks in masonry. An overview of FDEM is provided in [22]. The approach is also investigated with regard to in-plane and out-of-plane loaded masonry panels in [23–25], respectively.

Masonry structures usually show high compressive strength coupled with a negligible tensile capacity. Such behaviour is even more evident in historic buildings where the mortar layers have deteriorated with age. No-tension models are a valid alternative to investigate the mechanical behaviour of dry-joint masonry walls. The no-tension approach stems from the original idea of Heyman [26] and has been improved since the nineties [27,28] up to the very recent contributions both regarding vertical bearing piers [29] and for horizontally curved masonry shells [5,30–32]. The effect of highly localised compressive stress distribution within dry masonry has also been underlined experimentally [33] and theoretically [34–36].

* Corresponding author.
E-mail address: mlv@unife.it (V. Mallardo).

https://doi.org/10.1016/j.engstruct.2024.119220
Received 22 April 2024; Received in revised form 6 October 2024; Accepted 21 October 2024
Available online 9 November 2024

Recently, much effort has been devoted to the analysis of the influence of differential settlements on existing masonry structures. Such settlements can be either tunnelling-induced or due to natural or man-made detrimental effects that produce slow support displacements. Induced crack patterns affect the mechanical response of the masonry walls and represent a severe risk not only for life safety but also for the preservation of cultural heritage. Such effects have been investigated both experimentally [37–39] and numerically (mainly in 2D analyses) with different approaches: energy methods [40–43], limit analysis [44–47], rigid block model [48–50], FE method [51–53], finite-discrete element method [54,55]. All the contributions deal with 2D analysis. Historic masonry structures can often be regarded as an assemblage of independent 2D walls, especially w.r.t. differential settlements [56].

All of the aforementioned contributions do not consider the inclusion of soil in the structural analysis, i.e. settlement is typically treated as a predefined boundary condition, and the interfacial interaction between masonry construction and soil is disregarded. The main goal of the present paper is to present a novel approach to directly considering the soil–structure interaction while computing the mechanical response of masonry walls subjected to general external loading conditions and in unilateral contact with the underneath soil.

The proposed approach involves the computation of the fundamental solution due to unit point loads within the half-plane and its application to the BEM [57]. The procedure's advantages are twofold: the discretisation is limited to the wall-soil interface, and the soil's infinite behaviour is automatically included in the fundamental solution. The soil is modelled as a semi-infinite elastic domain without loss of generality, but the approach will be extended to more complicated configurations in future work. The contact between masonry and soil is modelled as unilateral in the normal direction and following a Mohr–Coulomb associated friction law in the tangential direction. An iterative solution is developed to apply proper unilateral contact conditions on the wall-soil interface.

The present paper is organised as follows. Section 2 describes the rigid, no-tension model for the masonry, and the corresponding boundary value problem is solved through the minimum of the total complementary energy. The elasticity of the masonry is concentrated at the brick-brick interfaces. Section 3 details the integral equations governing the mechanical response of the elastic half-plane under generic boundary conditions and their numerical implementation. Section 4 shows how masonry and soil's unilateral (with friction) contact conditions are numerically computed. In Section 5, numerical examples are presented and critically discussed to showcase the method's potential. Section 6 draws main conclusions and future works.

2. Masonry model

The following section outlines the mechanical model adopted for masonry, which is based on the so-called Normal Elastic No-Tension (NENT) material [5]. It considers the unilateral contact between bricks and includes a finite friction capacity. The model is introduced theoretically, along with the variational criterion adopted to solve the associated boundary value problem. Subsequently, the problem is discretised and formulated as a convex optimisation problem. The NENT mathematical formulation and its application to masonry have been studied in different contributions. For instance, constitutive equations and the existence of an energy function are discussed in [58]. In [59], the existence of a solution in the case of 2D NENT is demonstrated under the small strain assumption. A detailed study on the compatibility conditions to be satisfied by the external loads is given in [60]. In [61–63], the crushing in masonry is modelled for the first time as a perfectly plastic behaviour, i.e., by considering a convex elastic domain coupled with a normality law.

2.1. Theoretical model

The model adopted to describe the mechanical behaviour of the masonry is an extension of [40,64]. The reader is referred to [65] for the notation here adopted. A 2D continuum masonry structure $\Omega \in R^2$ is partitioned into a finite number of elastic elements Ω_i whose interaction is unilateral and follows a Mohr–Coulomb associated friction law (Fig. 1). Each boundary Γ_I of Ω_j is assumed regular (i.e. Lipschitz continuous). The two open, disjoint parts Γ_U, Γ_F represent the constrained and loaded part of the boundary of Ω, while $\hat{\Gamma}$ is the union of the internal interfaces Γ_I for $I \in \{1, \dots, M\}$. Either displacements $\mathbf{u} = \bar{\mathbf{u}}$ on Γ_U or transactions $\mathbf{s}(\mathbf{T}) = \bar{\mathbf{s}}$ on Γ_F are prescribed, with $\mathbf{s}(\mathbf{T})$ denoting the emerging stress tensor on the boundary.

In the case of singular stress crossing the boundary in $\mathbf{x} \in \partial\Omega$, the trace has to be written as $s(\mathbf{T}) = P\delta(\mathbf{x})\mathbf{t}$, where the scalar P is the magnitude of the singular stress and $\mathbf{t}$ is a unit vector directed as the uniaxial stress $\mathbf{T}$ [60,66]. This equation also holds on each internal interface. The spaces of admissible stresses and displacements are defined so that they have to account for singular stresses and displacement jumps, represented by Dirac delta distributions having $\hat{\Gamma}$ as support [62,67]. Indeed, to model the unilateral behaviour on the internal interfaces, it is required that the displacement field $\mathbf{u}$ can be singular on each Γ_I showing jumps $\Delta\mathbf{u}^I$ that can be decomposed in their normal $\Delta\mathbf{u}^I_N$ and tangential $\Delta\mathbf{u}^I_T$ components [40]. With $|\cdot|$ the $L2$ norm, the set of admissible displacements reads:

$$\mathcal{K} = \{\mathbf{u} \in SBV(\Omega_j) \text{ for } j = 1, \dots, n \text{ s.t. } |\Delta\mathbf{u}^I_N| \geq 0 \text{ on } \Gamma_I \text{ and } \mathbf{u} = \bar{\mathbf{u}} \text{ on } \Gamma_U\}, \tag{1}$$

with SBV the set of functions with bounded variation [68]. Friction conditions read:

$$\text{if } |\mathbf{S}^I_T| < \mu |\mathbf{S}^I_N| \text{ then } |\Delta\mathbf{u}^I_T| = 0, \tag{2a}$$

$$\text{if } |\mathbf{S}^I_T| = \mu |\mathbf{S}^I_N| \; \exists \lambda \geq 0 \text{ s.t. } \Delta\mathbf{u}^I_T = -\lambda\mathbf{S}^I_T \text{ and } \Delta\mathbf{u}^I_N = \mu\Delta\mathbf{u}^I_T, \tag{2b}$$

being μ the friction coefficient and $\mathbf{S}^I_N$ and $\mathbf{S}^I_T$ the unknown, normal and tangential force distributions on Γ_I. The symmetric stress tensor must belong to the Mohr–Coulomb cone C, i.e., $\mathbf{T} \in C \subset Sym^-$. To allow for singular stresses, $\mathbf{T}$ has to belong to SBM, being SBM the set of functions with bounded measures [68]. Therefore, the set of admissible stress fields reads:

$$\mathcal{H} = \{\mathbf{T} \in SBM \;:\; \text{div}\mathbf{T} + \mathbf{b} = \mathbf{0}, \; T \in C, \; s(\mathbf{T}) = \bar{\mathbf{s}} \text{ on } \Gamma_F\}. \tag{3}$$

A solution of the boundary value problem (BVP) is represented by a stress $\mathbf{T} \in H$ and a displacement $\mathbf{u} \in K$ fulfilling Eqs. (2). The Gauss–Green theorem for an elastic material reads:

$$a(\mathbf{u}, \mathbf{u} - \mathbf{u}^*) = \int_\Omega \mathbf{b} \cdot (\mathbf{u} - \mathbf{u}^*) d\Omega + \int_{\Gamma_F} \bar{\mathbf{s}} \cdot (\mathbf{u} - \mathbf{u}^*) d\Gamma + \sum_{i=1}^{M} \int_{\Gamma_I} \left[\mathbf{S}^I_N \cdot (\Delta\mathbf{u}^I_N - \Delta\mathbf{u}^{I,*}_N) + \mathbf{S}^I_T \cdot (\Delta\mathbf{u}^I_T - \Delta\mathbf{u}^{I,*}_T)\right] d\Gamma, \tag{4}$$

with $a(\mathbf{u}^*, \mathbf{u})$ a quadratic functional that doubles the elastic energy and $\mathbf{u}^*$ is the displacement solving the BVP. The model accounts for elastic energy in compression. For instance, it may be diffused in the bricks or, without lack of generality, lumped in with the interfaces as also done by commercial solvers [69]. In the present paper, the elastic energy in compression is adopted to model the compressive elastic response of the masonry and lumped in with the assembly interfaces. From the problem at hand, it can be easily shown that the following variational criterion holds:

$$A(\mathbf{T}^*, \mathbf{T} - \mathbf{T}^*) \geq \int_{\Gamma_U} \bar{\mathbf{u}} \cdot (\mathbf{T}\mathbf{n} - \mathbf{T}^*\mathbf{n}) d\Gamma \quad \forall \mathbf{T} \in \mathcal{H}, \tag{5}$$

with A doubling the complementary elastic energy, and T^* is the stress tensor corresponding to a solution of the BVP. Relation (5) is equivalent to the following minimisation problem:

$$\mathbf{T}^* = \text{argmin}\{\Pi_c(\mathbf{T})_{\mathbf{T} \in \mathcal{H}}\} \quad \text{with } \Pi_c(\mathbf{T}) = \frac{1}{2}A(\mathbf{T}, \mathbf{T}) - \int_{\Gamma_U} \bar{\mathbf{u}} \cdot \mathbf{T}\mathbf{n} d\Gamma, \tag{6}$$

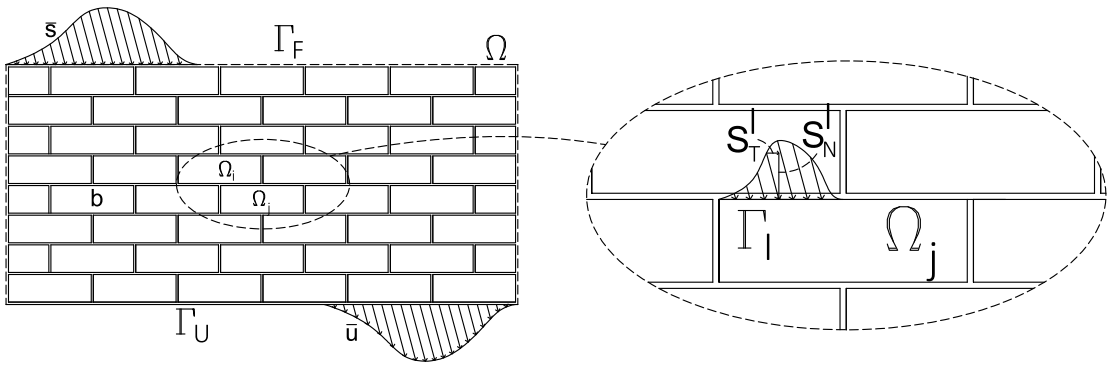

Fig. 1. Multiple elastic bodies subjected to body force $\mathbf{b}$, prescribed boundary displacements $\bar{\mathbf{u}}$ on Γ_U, friction boundary condition on Γ_I and surface force $\bar{\mathbf{s}}$ on Γ_F; $\mathbf{S_N}$, $\mathbf{S_T}$ are normal and tangential contact pressure.

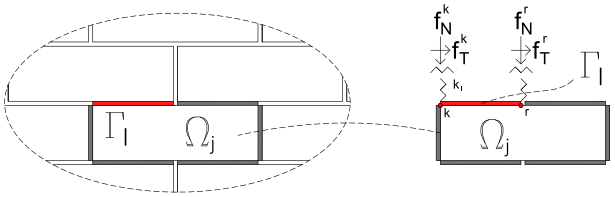

Fig. 2. Numerical discretisation of the interface tractions being k and r two generic nodes.

which provides the solution to the friction BVP [65], with $\Pi_c(\mathbf{T})$ the total complementary energy (TCE).

2.2. Numerical discretisation

This subsection illustrates the numerical discretisation of the TCE minimum problem (6), considering a masonry domain partitioned into dry blocks exhibiting a typical interlocked pattern. In many discrete element modelling strategies [70], a commonly used numerical approach to account for the blocks' elastic compressive behaviour is to consider them rigid and lump their entire elastic response at the block interfaces, using appropriate values for the tangential and normal joint stiffness (see Fig. 2). Various authors have investigated different values for joint stiffness, considering factors such as block size and interface properties. The reader is referred to [69] and references therein for more detailed information. It is important to note that once the elastic response has been concentrated at the interfaces between the elements, the numerical formulation of friction conditions (Eq. (2)) needs to be slightly rearranged. Let us consider the following additive decomposition of the displacement jumps over the interfaces between the blocks:

$$\Delta\mathbf{u}_N^I = \Delta\mathbf{u}_N^{I^e} \quad , \quad \Delta\mathbf{u}_T^I = \Delta\mathbf{u}_T^{I^e} + \Delta\mathbf{u}_T^{I^p} \, , \tag{7}$$

being $|\cdot|^p$ and $|\cdot|^e$ the latent and elastic components of the displacement jumps, respectively. It should be noted that relation $(7)^1$ implies a purely elastic interface behaviour in compression, while $(7)^2$ assumes an elastic behaviour along the tangential direction till the sliding failure $\Delta\mathbf{u}_T^{i^p}$ is activated because of the Mohr–Coulomb yielding criterion. Therefore, relations (2) have to be rewritten (for instance for node k) as :

$$\text{if } |\mathbf{f}_T^k| \leq \mu\, |\mathbf{f}_N^k| \text{ then } \Delta\mathbf{u}_T^{k^e} = \frac{\mathbf{f}_T^k}{k_I} \text{ and } \Delta\mathbf{u}_T^{k^p} = \mathbf{0} \, , \tag{8a}$$

$$\text{if } |\mathbf{f}_T^k| = \mu\, |\mathbf{f}_N^k| \; \exists \lambda \geq 0 \text{ s.t. } \Delta\mathbf{u}_T^{k^p} = -\lambda \mathbf{f}_T^k \text{ and } \Delta\mathbf{u}_N^{k^p} = \mu \Delta\mathbf{u}_T^{k^p} \, , \tag{8b}$$

being μ the friction coefficient, k_I the interface stiffness and $\mathbf{f}_N^k$, $\mathbf{f}_T^k$ nodal forces occurring on the node k.

For a fully 3D numerical model, the TCE minimum is modelled using the following second-order cone programming (SOCP) in a typical concave contact formulation (^{t} means transpose):

$$\text{Minimise} \quad -\mathbf{B}_s\mathbf{F}^t\bar{\mathbf{U}} + \frac{1}{2}\mathbf{F}^t\mathbf{A}\mathbf{F} \tag{9a}$$

$$\text{s.t.} \quad \mathbf{A}_{eq}\mathbf{F} + \mathbf{b} + \mathbf{A}_q\mathbf{q}_p = \mathbf{0} \tag{9b}$$

$$|\mathbf{f}_T^k| \leq \mu \mathbf{f}_N^k \text{ for } k = 1, \ldots, n_{nodes} \tag{9c}$$

where $\mathbf{F}$ is a vector collecting the internal nodal forces $\mathbf{f}_N^k$, $\mathbf{f}_T^k$ occurring at each node k; $\mathbf{F}_s = \mathbf{B}_s\mathbf{F}^t$ is the emerging traction vector obtained using the extract operator $\mathbf{B}_s$; $\mathbf{b}$ is the vector modelling the volume forces as lumped in with the block' centroids, and $\mathbf{q}_p$ is a vector representing additional concentrated loads translated to the block's centroids using the operator $\mathbf{A}_q$. Looking at the constraints, Eq. (9b) enforces the equilibrium of the elements through the equilibrium matrix $\mathbf{A}_{eq}$, while relation (9c) represents the Mohr–Coulomb relation among tangential and normal forces scaled down by the friction coefficient μ. Eq. (9c) represents n second-order cone constraints, with n the total number of nodes.

The objective function is the sum of a quadratic and a linear form and represents the TCE. Indeed, its linear part models the opposite of the work of emerging stresses and support displacements. At the same time, the quadratic function enforces the interface's elastic behaviour through the compliance matrix $\mathbf{A}$. The reader should note that the matrix $\mathbf{A}$ accounts for the geometrical distribution of the interface properties over the digital domain. Their values are evaluated according to [69]. Due to the quadratic form, the objective function remains convex but nonlinear. To maintain linearity, the quadratic form can be incorporated into the constraints as cones, while additional slack variables replace its contribution to the objective function. It is important to note that in 2D numerical models, the Mohr–Coulomb constraints become linear. Nevertheless, introducing the quadratic form into the constraints to model the elastic interface behaviour leaves the optimisation problem as a SOCP problem. The dual displacements can be obtained from the Lagrange multiplier associated with the TCE optimisation problem. For more detailed information, the reader can refer to [29], where a Heymanian-associated flow rule is adopted without losing generality.

3. Half-plane fundamental solution and numerical implementation

The stress distribution due to point loads applied within the isotropic half-plane was presented by Melan [71]. The solution in terms of stresses generated by a point force normal to an elastic half-plane is also known as Flamant solution [72,73]. The implementation of [71] in the BEM is provided in [57]. The procedure is here briefly described for the sake of clarity.

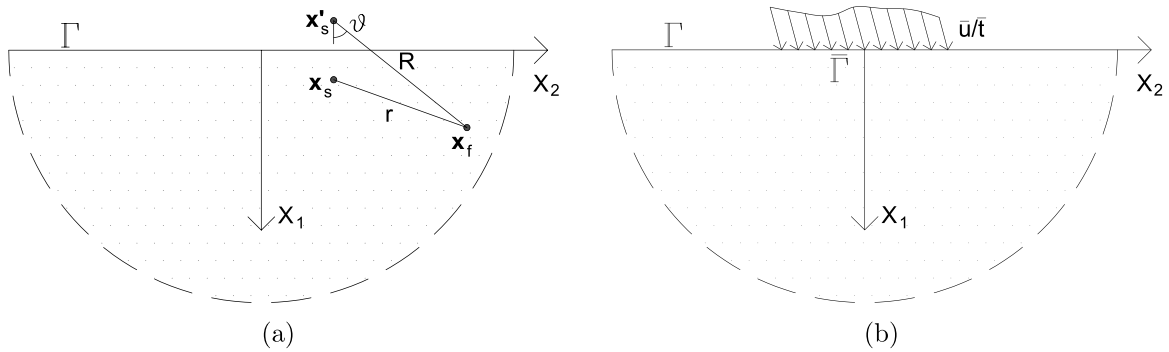

Fig. 3. (a): Unit point load in $\mathbf{x}_s$ within the half plane $X_1 = 0$, its image $\mathbf{x}'_s$ and field point $\mathbf{x}_f$. (b): Prescribed displacements or tractions on $\bar{\Gamma} \in \Gamma$.

First of all, it can be shown that Melan's fundamental solution is the sum of the classical infinite fundamental solution due to Kelvin plus a complementary part:

$$U_{ij} = u^k_{ij} + u^c_{ij}\,, \qquad T_{ij} = t^k_{ij} + t^c_{ij}\,, \tag{10a}$$

The former is (in Einstein's notation):

$$u^k_{ij}(\mathbf{x}_s, \mathbf{x}_f) = -\frac{1}{8\pi(1-\nu)\mu}\left[(3-4\nu)\log r\delta_{ij} - r_{,i}r_{,j}\right] \tag{11a}$$

$$t^k_{ij}(\mathbf{x}_s, \mathbf{x}_f) = -\frac{1}{4\pi(1-\nu)r}\left\{\left[(1-2\nu)\delta_{ij} + 2r_{,i}r_{,j}\right]\frac{\partial r}{\partial \mathbf{n}} - (1-2\nu)(r_{,i}n_j - r_{,j}n_i)\right\} \tag{11b}$$

where $\mathbf{t}$ is the traction in $\mathbf{x}_s$ on the plane with normal $\mathbf{n}$, ν and $\mu = \frac{E}{2(1+\nu)}$ are the Poisson's ratio and the shear modulus, respectively (E being Young's modulus), $r = (r_i r_i)^{\frac{1}{2}}$ is the distance between load (or source) point $\mathbf{x}_s$ and field point $\mathbf{x}_f$, δ is the Kronecker delta, the subscript $,l$ means derivative with respect to X_l. The complementary part is provided by:

$$u^c_{ii}(\mathbf{x}_s, \mathbf{x}_f) = \frac{1}{8\pi\mu(1-\nu)}\left\{\frac{(3-4\nu)r_i^2 + 2\gamma_i X_1(\mathbf{x}_s)X_1(\mathbf{x}_f)}{R^2} - \gamma_i\frac{4X_1(\mathbf{x}_s)X_1(\mathbf{x}_f)\bar{r}_i^2}{R^4} - 8\left[(1-\nu)^2 - (3-4\nu)\right]\log R\right\} \tag{12a}$$

$$u^c_{jk}(\mathbf{x}_s, \mathbf{x}_f) = \frac{(3-4\nu)}{R^2} - 4\gamma_j X_1(\mathbf{x}_s)x_1(\mathbf{x}_f)R_1 r_2 + 4\gamma_j(1-\nu)(1-2\nu)\theta \tag{12b}$$

where $\mathbf{x}'_s$ is the image of $\mathbf{x}_s$ with respect to Γ (i.e. the plane $X_1 = 0$), $\bar{r} = R$ if $i = 1$ and $\bar{r} = r$ if $i = 2$, $\gamma_l = (-1)^l$ with $l = i, j$ and other terms are depicted in Fig. 3a. It is worth underlining that such a fundamental solution automatically satisfies the traction-free condition on Γ when $\mathbf{x}_s$ is located internally. Furthermore, the complementary fundamental tractions are provided by:

$$t^c_{ij}(\mathbf{x}_s, \mathbf{x}_f) = \sigma^c_{jki}(\mathbf{x}_s, \mathbf{x}_f)n_k(\mathbf{x}_s)\,, \tag{13}$$

where the expression of the fundamental stresses σ^c_{jki} can be found in [57,74].

Expressions (11)–(13) refer to plane strain; they are valid for plane stress too if ν is replaced by $\bar{\nu} = \nu/(1+\nu)$. The implementation of the governing boundary integral equation can follow the same pattern of the classical BEM (i.e. by Somigliana's identity) by specialising it for $\mathbf{x}_s \to \boldsymbol{\xi} \in \Gamma$:

$$c_{ij}(\boldsymbol{\xi})u_{ij}(\boldsymbol{\xi}, \mathbf{x}_f) + \fint_\Gamma T_{ij}(\boldsymbol{\xi}, \mathbf{x}_f)u_j(\mathbf{x}_f)d\Gamma(\mathbf{x}_f) = \int_\Gamma U_{ij}(\boldsymbol{\xi}, \mathbf{x}_f)t_j(\mathbf{x}_f)d\Gamma(\mathbf{x}_f)\,, \tag{14}$$

where $\fint$ stands for Cauchy principal integral and $c_{ij} = \delta_{ij}/2$ on smooth surfaces. Singularity issues related to Eq. (14) are discussed in many contributions (for instance, [75]).

The numerical implementation of Eq. (14) follows the classical collocation procedure. Due to the special property of the fundamental solution adopted, only is discretised the loaded part $\bar{\Gamma}$ of Γ (either $u_i = \bar{u}_i$ or $t_i = \bar{q}_i$, see Fig. 3b). Therefore, the discretisation on Γ involves only the interface contact zone between masonry wall and soil, implying the discretisation of the traction-free part of the boundary, i.e. $\Gamma - \bar{\Gamma}$, to be unnecessary. Finite cavities can be easily included by involving their boundary in the discretisation step. It is worth underlining that the solution automatically satisfies the regularity condition at infinity. For the present implementation, linear piecewise functions are chosen to interpolate displacements and tractions over the boundary elements. After the collocation technique [75] and application of the boundary conditions ($t_i = \bar{t}_i$) following the iterative procedure described in the next Section, the final governing system of the equation is:

$$\mathbf{Hu} = \mathbf{Gt} \implies \mathbf{Hu} = \mathbf{b}\,, \tag{15}$$

where $\mathbf{H}$ collects the l.h.s integrals of (14) and $\mathbf{G}$ the r.h.s. ones. At each iteration of the iterative procedure, pressure and tangential tractions are imposed, and displacements on $\bar{\Gamma}$ are computed. Displacement or stress in any point inside the half-plane or on $\Gamma - \bar{\Gamma}$ can be computed as a post-processor step [75]. Fig. 4 shows a comparison between analytical [76] and BEM vertical displacements under symmetrical constant load $\bar{q}_1 = 10$ applied in $X_1 \in (-b, b)$ with $b = 5$, and $E = 1000$, $\nu = 0.3$ for the soil, all in compatible units. Four linear boundary elements (two for each symmetric part) are sufficient to provide a precise solution. Due to the well-known non-uniqueness of displacements in 2D analysis, the vertical displacements are given with reference to the corresponding displacement of the origin. Such a feature is not an issue as the difference is a rigid body motion that can be detracted without affecting the compatibility and equilibrium relations at the interface. For instance, a simple rigid translation can transform the solution depicted in Fig. 4 into the one in Fig. 5.

4. Soil–structure interaction: coupled approach

This Section provides detailed information about equilibrium and compatibility conditions that need to be satisfied over the foundation line between masonry and soil in order to model their non-smooth mechanical interaction accurately. It is worth noting that historic masonry buildings are typically built by layering the brick–mortar assembly directly on the soil without interlaying any bending-resistant beam. The masonry is modelled as an assembly of rigid blocks, as mentioned in Section 2. Furthermore, the contact between masonry and soil must comply with unilateral conditions and an associated Mohr–Coulomb friction law.

To ensure that equilibrium and unilateral contact conditions are met, the interface between the masonry and soil (referred to as the *foundation line* from now on) needs to be appropriately modelled. To this aim, additional rigid blocks are employed on the foundation line. The masonry structure is assumed to be subjected to body forces as well as contact forces represented by vertical and horizontal actions. Horizontal forces, for instance, may represent seismic actions. Two

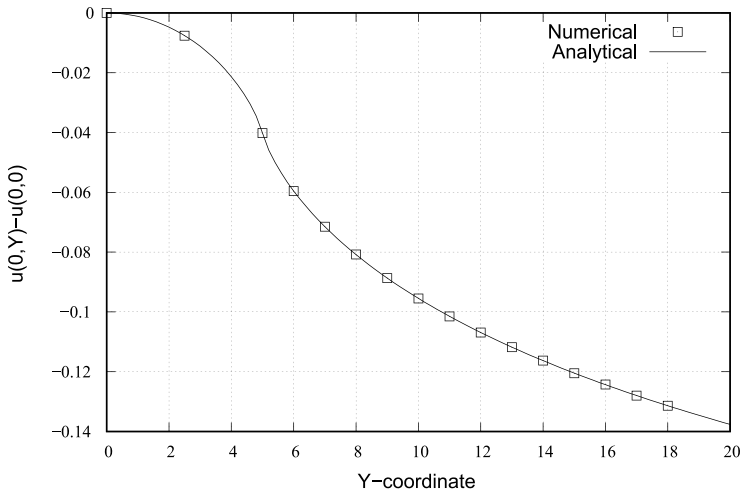

Fig. 4. Comparison of vertical displacements under constant load.

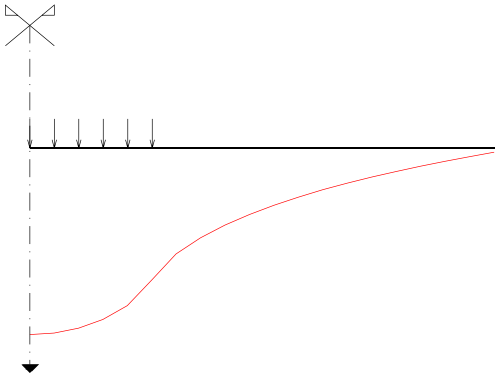

Fig. 5. Uniform pressure applied: undeformed (straight line —) and BEM ($u(x,0) - u(4b,0)$) deformed (—) boundary.

iterative numerical strategies are developed and compared to calculate the mechanical response of the masonry-soil coupled system.

Remark. The numerical model adopted for masonry is a full 3D model, while the soil model is 2D. The soil model can account for either plane stress or plane strain conditions, and in this paper, the plane strain assumption is adopted for all numerical applications. However, the investigation is restricted to 2D symmetric cases under in-plane loading conditions, such as walls, facades, and arched structures. In such cases, it is important to highlight that the proposed approach provides a reasonable representation of the actual behaviour as:

- the interface elasticity of the masonry model is concentrated in normal and tangential springs. Under in-plane loading conditions, the masonry exhibits only the in-plane response, as the tangential springs are not activated;
- the forces transmitted to the soil are exclusively in-plane forces;
- the corresponding (plane-strain) solution for the soil provides displacements without any (non-constant) component along the orthogonal (out-of-plane) direction. Although out-of-plane stresses may occur in the soil, they do not manifest on the interface plane and, therefore, do not affect the displacement boundary conditions applied to the masonry during the iterative process.

4.1. Non-linear interface conditions

Due to the unilateral nature of the soil–structure interaction, any contact model must consider potential partial detachments along the foundation line; hence, it must be unilateral. A bilateral contact approach cannot accurately represent the unilateral soil–structure behaviour, as it fails to capture potential detachments. In the present research, the unilateral non-smooth contact over the foundation line is modelled by considering the tractions transferred from the masonry to the soil as well as the soil deformation, which results in displacements that must be applied to the masonry and can, in turn, influence the masonry response and the resulting transferred tractions. This problem is addressed by defining an iterative procedure that not only accounts for the unilateral contact between the masonry and the half-plane (soil) but also considers the unilateral response of the masonry. To the authors' knowledge, all contributions related to masonry subjected to settlements, such as [37,39,48–52,54,77], do not directly account for coupled soil–structure behaviour. The following subsections describe the iterative algorithm implemented to evaluate the non-smooth soil–structure interaction, considering both the masonry's unilateral and the soil's elastic response. The algorithm calculates the tractions and displacements exchanged between masonry and soil in each iteration. Two different strategies are implemented and explored to model these data.

Specifically, the interaction between masonry and soil is modelled using additional rigid (red) blocks with negligible height in between the masonry structure and the soil, which serve as supports for the masonry structures (Fig. 6).These supporting red blocks are used to apply displacement-like boundary conditions to the masonry base once the deformation of the half-plane soil is evaluated. As clarified below, for the first contact strategy, they are also used to transfer the tractions exerted by the masonry to the soil.

Referring to the transmission of traction from the masonry to the soil and remembering that the masonry model is based on a concave contact formulation (Fig. 2), two contact strategies are implemented and explored as illustrated by Fig. 6:

- contact strategy 1 directly uses the supporting red blocks beneath each cyan masonry block. The forces transmitted by each cyan block are summed at each contact point and then distributed over the corresponding influence area to evaluate the surface traction to be applied to the half-plane soil (see Section 4.3.1 for details);
- contact strategy 2 models an additional yellow block between supports and structure as illustrated in Fig. 6. The two forces transmitted from the cyan to the yellow block through the two endpoints are used to model the unilateral contact pressures using

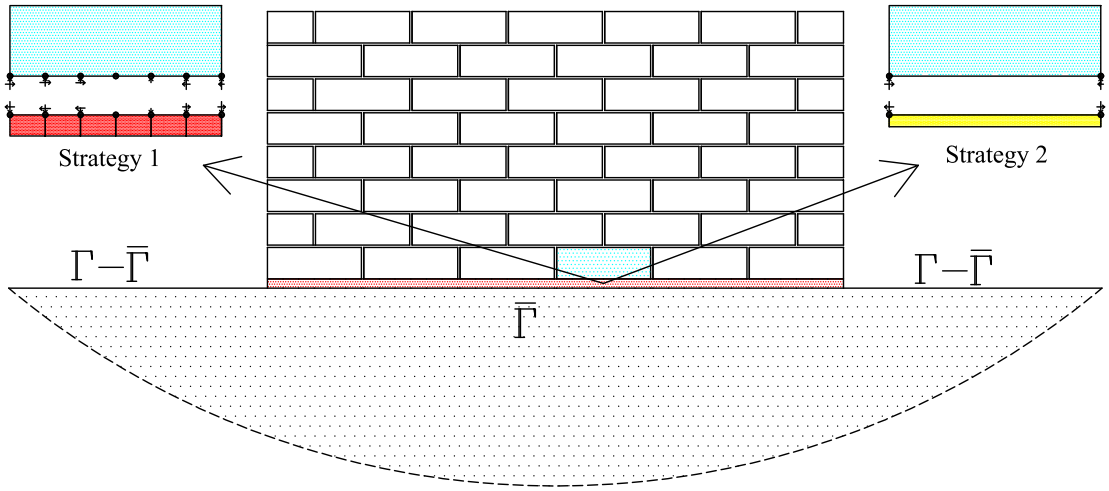

Fig. 6. Masonry-soil system: the generic masonry block is depicted in cyan, while additional red blocks are adopted as supports to model the soil–structure contact. (For interpretation of the references to colour in this figure legend, the reader is referred to the web version of this article.)

the 3u rule in a post-processing phase (see Section 4.3.2 for details).

A similar approach is adopted to transfer the displacement field from the soil to the masonry. As detailed in Section 3, the adopted soil model provides a displacement field for the boundary layer of the soil, represented as a continuous function by the boundary mesh. The displacement field on the masonry is thus discretised through a set of kinematic parameters, i.e., by horizontal and vertical displacements and a rotation with respect to the centre of gravity of each red block (see Section 4.2 for details). In this sense, displacement-like boundary conditions are enforced using a numerical strategy similar to Strategy 1 for tractions, as no other strategies are possible. In conclusion, additional rigid blocks are introduced at the foundation line for two purposes:

- to transmit tractions from the masonry to the soil, meaning that nodal boundary reactions of the wall are computed and then applied as external tractions to the half-plane model;
- to transfer the imposed displacement field from the soil to the masonry.

It is worth highlighting that the contact between masonry blocks and the additional (red and yellow) supports is still modelled as elastic unilateral in compression and elastic bilateral along the tangential interface direction. A finite friction capacity is also assumed based on the Mohr–Coulomb yielding criterion.

In summary, at each iteration, the masonry mechanical problem is solved by minimising the discredited version of the minimin of complementary energy (9), whose solution yields the nodal forces $\mathbf{f}^i = (f_N^i, f_T^i)$, being f_N^i and f_T^i the normal and tangential components, respectively. After that, the tractions over the foundation line are evaluated using either contact strategy 1 or 2 and used as data for the half-plane model, which yields soil displacements over the foundation line. These displacements are discredited as described above and used to impose foundation settlements on the masonry.

4.2. Compatibility conditions

This Section describes the numerical procedure to transfer displacements from the half-plane to the masonry model. The displacement solution of the half-plane subjected to prescribed tractions needs to be transferred to the masonry model. The half-plane displacement solution is provided in terms of $\mathbf{u} = (u_N, u_T)$ and is then linearly interpolated and lumped to the masonry supports as shown in Fig. 7. For instance, the rigid body motion of the red block in between the nodes l and l+1 (with $l = 1, \dots, n$ being n the number of nodes of the half-plane problem) can be expressed as follows:

$$\boldsymbol{\delta}_l = \frac{\mathbf{u}_{l+1} + \mathbf{u}_l}{2}\,, \quad \phi_l = \frac{u_{N_{l+1}} - u_{N_l}}{a}\,, \tag{16}$$

with $\boldsymbol{\delta}_l$ the displacement of the lth support determined by averaging the displacements of the adjacent nodes; ϕ_l the rotation of the red block at node l, which is obtained by calculating the difference in normal displacements between the adjacent nodes and dividing it by the spacing a between the nodes. Thus, the boundary displacements to apply to the masonry supports at the iteration i-th is:

$$\mathbf{u}_{m,i}^{\bar{\Gamma}} = (\boldsymbol{\delta}, \boldsymbol{\phi})_i^{\bar{\Gamma}}\,, \tag{17}$$

with $\boldsymbol{\delta}$ and $\boldsymbol{\phi}$ the vectors collecting support displacements $\boldsymbol{\delta}_l$ and rotations ϕ_l.

4.3. Equilibrium conditions

Once displacements are defined, the BVP solution is obtained by solving the SOCP (9). Its solution yields nodal forces $\mathbf{f}^i$ that must be transferred to the half-plane below through proper equilibrium conditions. Two different numerical strategies are considered, as outlined below.

4.3.1. Contact strategy 1

The first contact strategy, referred to as *strategy 1*, is obtained by spreading the masonry reactions as tractions in each half-plane node (Fig. 8), that is:

$$\mathbf{t} = -\frac{\mathbf{f}}{a\,s}\,, \tag{18}$$

where s is the masonry block's depth (assumed here as a unit), a represents the footprint length of each node (half on the left and half on the right for internal nodes, just half-length for the end nodes, see Fig. 8), $\mathbf{f}$ represents the contact force vector acting on the wall and $\mathbf{t}$ denotes the contact traction on the half-plane. It is worth recalling that the half-plane model linearly interpolates the tractions on adjacent nodes. The normal component is zero when the masonry detaches from the foundation line, excluding cases of dilatancy.

On the other hand, the tangential traction is locally bounded by the finite friction capacity as described in Section 2. Thus, the tangential traction can only be non-zero if the normal component is non-zero, as illustrated in Fig. 8. Consequently, the local (point-wise) condition $f_T^i \le \mu f_N^i$ is satisfied throughout the contact area.

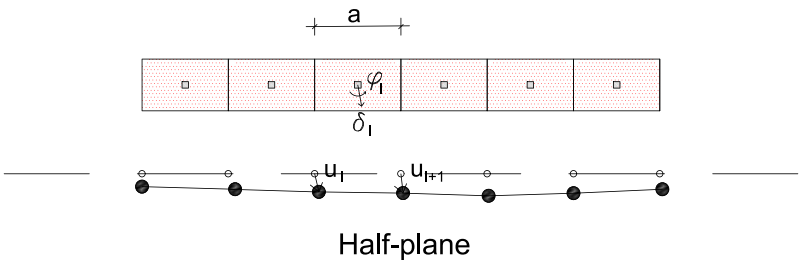

Fig. 7. Compatibility conditions between the masonry and soil involve the transmission of the half-plane displacement to the supports' Lagrangian parameters. (For interpretation of the references to colour in this figure legend, the reader is referred to the web version of this article.)

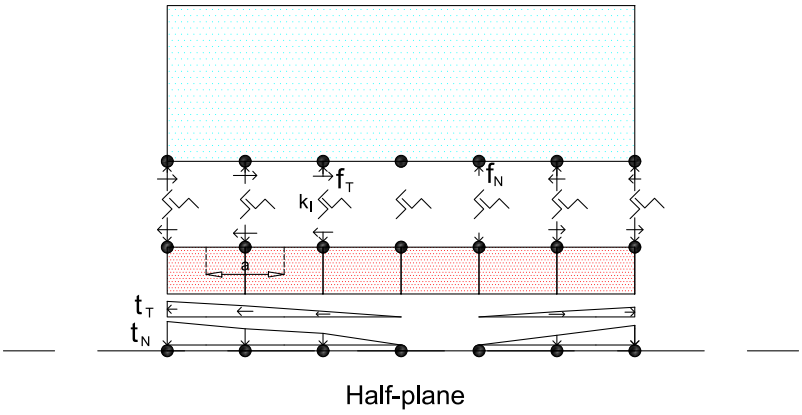

Fig. 8. Contact *strategy 1*: force interaction between masonry structure and soil. (For interpretation of the references to colour in this figure legend, the reader is referred to the web version of this article.)

4.3.2. Contact strategy 2

The second contact strategy computes the tractions to be transmitted to the half-plane differently. For numerical reasons, a layer of (yellow) blocks of negligible height is placed between the cyan blocks representing the masonry structures and the red blocks representing the foundation, as depicted in Fig. 9. The solution of minimum problem (9) yields nodal contact forces $\mathbf{f}$ between cyan and yellow blocks. Each cyan block is associated with a single (yellow) block placed directly beneath it, as depicted in Fig. 9. The nodal forces $\mathbf{f}$ are used to compute the stress state on the yellow block based on a linear, unilateral contact model. Using this information, a contact (i.e. active) area is defined. Referring to Fig. 9, the resultant $\mathbf{R}$ of the nodal forces is calculated as $\mathbf{R} = \mathbf{f}^l + \mathbf{f}^r$ with l and r symbolising the left and right corners of the blocks, respectively. The tangential component R_T of $\mathbf{R}$ is uniformly distributed over the contact zone of the half-plane interface. It is important to note that in Strategy 2, the finite friction capacity applies globally to the entire contact area in an integral sense rather than locally. The distribution of the normal traction over the half-plane, resulting from the normal component $R_N = \mathbf{R} \cdot \mathbf{n}$, depends on the eccentricity $e = \frac{f^r_N \ b/2 - f^l_N \ b/2}{R}$ with e positive if the resultant is located to the right of the brick's gravity centre. When $\|e\| \leq \frac{b}{6}$, the compressive tractions at the left (t^l_N) and right (t^r_N) corner are computed by:

$$t^l_N = \frac{R_N}{bs} - \frac{6Ne}{sb^2} \quad , \quad t^r_N = \frac{R_N}{bs} + \frac{6\,N\,e}{s\,b^2} \quad , \tag{19}$$

On the other hand, if $\|e\| > \frac{b}{6}$, the normal component t_N is distributed linearly over the contact zone $l = 3\,u$, where:

$$u = q\frac{b}{2} - e \qquad q = 1 \ \text{ if } f^l_N < f^r_N \quad \text{else } \ q = -1 \quad . \tag{20}$$

The length l is measured from the left corner if $f^l_N > f^r_N$, from the right corner otherwise.

4.4. Iterative algorithm

The interface between the masonry and soil is modelled as a unilateral in compression with a finite friction capacity, similar to problems encountered in crack analysis [78]. This coupled problem is inherently nonlinear and is solved through an iterative procedure that updates the boundary conditions until the final solution is achieved. The developed algorithm is summarised in Fig. 10.

The first step is to compute the nodal contact forces $\mathbf{f}^{\bar{\Gamma}}_0$ by solving the minimum problem (9), considering given external loads and homogeneous boundary displacements (fixed foundation, i.e., $(\boldsymbol{\delta}, \boldsymbol{\phi})^{\bar{\Gamma}} = \mathbf{0}$). These forces are then transferred to the soil interface using either Eq. (18) or Eqs. (19)–(20), depending on the contact strategy adopted. The corresponding soil displacement on the half-plane boundary is computed using Eq. (15). This displacement field is then discretised and applied to the masonry supports using Eq. (16). The solution of the updated masonry BVP thus provides new nodal contact forces.

The procedure continues iteratively, computing the displacement field on the soil, $\mathbf{u}^{\bar{\Gamma}}_i$, and the interface forces, $\mathbf{f}^{\bar{\Gamma}}_i$, transmitted by the masonry to the soil along the foundation line.

Referring to the generic vector $\mathbf{x}$ representing data measured over the foundation line, the error between iteration $i-1$ and i is evaluated using the normalised root mean square error as:

$$\text{err}^i_x = \frac{1}{|\ \max(\mathbf{x}^{i-1}) - \min(\mathbf{x}^{i-1})\ |} \sqrt{\frac{\sum_{j=1}^{n}(x^i_j - x^{i-1}_j)^2}{n}}\,, \tag{21}$$

with n the number of nodes of the foundation line, x^i_j the jth component of $\mathbf{x}$ at the iteration i, and:

$$\max(\mathbf{x}^i) = \max_{j=[1,\dots,n]} x^i_j \quad , \quad \min(\mathbf{x}^i) = \min_{j=[1,\dots,n]} x^i_j\,. \tag{22}$$

The iterative loop ends if, at iteration i, the following four conditions are simultaneously met:

$$\text{err}^i_{\mathbf{f}_\text{N}} \leq \text{tol}_{\mathbf{f}_\text{N}} \quad , \text{err}^i_{\mathbf{f}_\text{T}} \leq \text{tol}_{\mathbf{f}_\text{T}} \quad , \text{err}^i_{\mathbf{u}_\text{N}} \leq \text{tol}_{\mathbf{u}_\text{N}} \quad , \text{err}^i_{\mathbf{u}_\text{T}} \leq \text{tol}_{\mathbf{u}_\text{T}}\,, \tag{23}$$

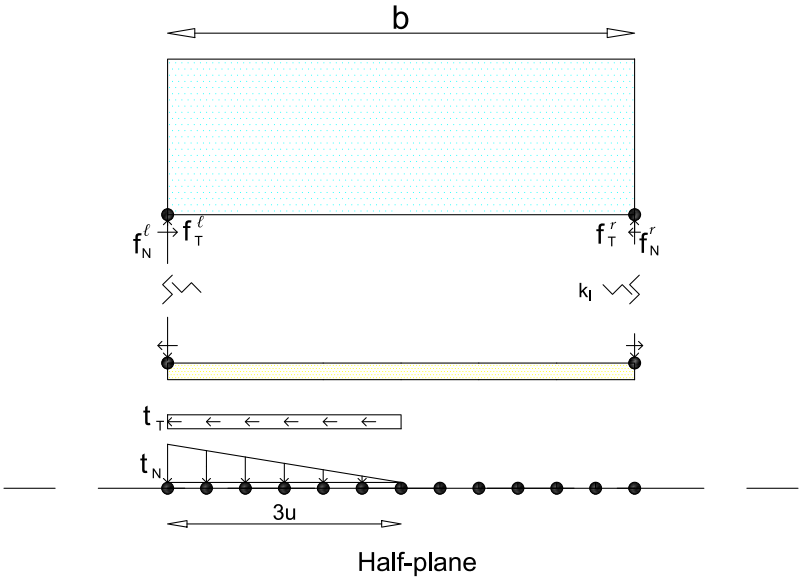

Fig. 9. Contact *strategy 2*: force interaction between masonry structure and soil. (For interpretation of the references to colour in this figure legend, the reader is referred to the web version of this article.)

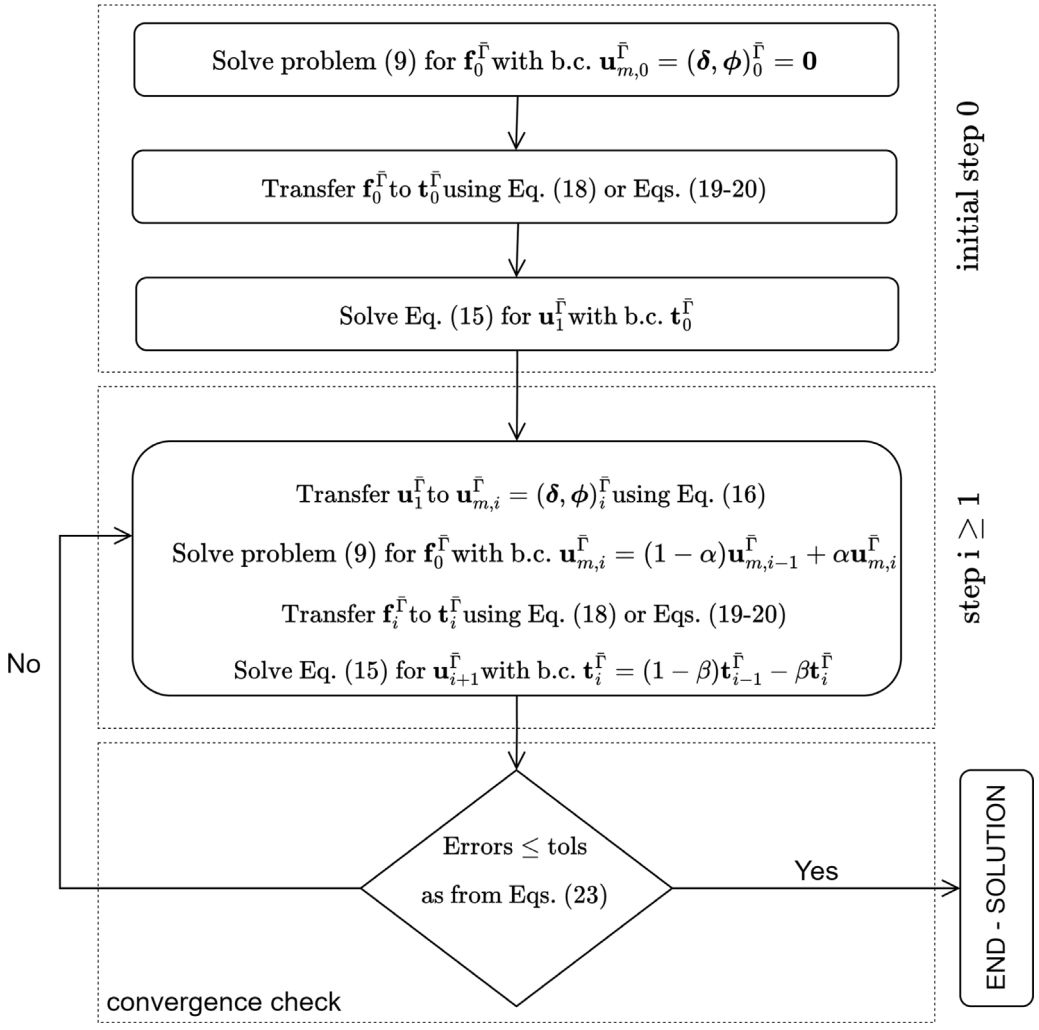

Fig. 10. Flowchart of the iterative scheme for the soil–structure interaction.

where the errors, evaluated by mapping relation (21) to both the normal and tangential components of the transmitted forces and soil displacements, must be smaller than prescribed numerical tolerances $\text{tol}_{(\cdot)}$.

To speed the convergence up and improve efficiency, an extension of the technique proposed in [79], originally designed for linear problems, is implemented: at each iteration of the algorithm, the boundary conditions (displacement type on the masonry, traction type on the soil) are updated as a linear combination (using parameters α and β) of the ith and $(i-1)$th values. In the numerical examples, α and β are determined through a preliminary parametric analysis.

5. Numerical applications

To highlight the efficiency of the proposed coupled approach with respect to traditional methods, this Section illustrates the results obtained on two simple but meaningful structural typologies, such as a panel and a semicircular arch. All computational analyses are performed using an in-house Python code implementing the numerical model illustrated in Section 2.2. The solutions are obtained on an agile laptop with an AMD Ryzen 7 5700U and using Mosek as optimisation solver [80]. The numerical solutions are obtained adopting $k_n = 10^9$ kN/m^3, $k_t = 3 \cdot 10^8$ kN/m^3 between bricks, and $k_n = 10^8$ kN/m^3, $k_t = 5 \cdot 10^7$ kN/m^3 between bricks and soil. It must be pointed out that the results are not affected by reducing the brick-brick stiffnesses, as also shown in [69].

The first application focuses on a rectangular masonry panel resting on elastic soil and subjected to two loading conditions (Section 5.1). In particular, by focusing on the contact footprint area between the masonry panel and the soil, the results explore the differences between contact strategies 1 and 2 and their deviations from the conventional scenario of a fixed, undeformable foundation. Section 5.2 looks at a semicircular arch, focusing on its behaviour under a non-symmetric loading condition. This application is a pilot case to demonstrate the proposed strategy's advantages and relevance in a common yet significant case, such as an arch, a paradigmatic example of a masonry curved structure.

Before proceeding with the examples described above, it would be useful to benchmark the adopted masonry model when compared with the results available in the literature for fixed foundations. A 15-voussoirs semicircular arch is considered. The collapse mechanism and corresponding value can be computed by applying iteratively the procedure described in Section 2.2 to maximise the horizontal multiplier λ or by reformulating the problem in a classical limit analysis sense as detailed in [81]. Fig. 11a shows the collapse mechanism for an arch with $t/r = 0.18$ with t the thickness and r the mean radius. Fig. 11b shows the behaviour of the horizontal load multiplier versus t/r. The results are identical to what is presented in [82], demonstrating the reliability of the adopted numerical masonry model. For further details and comparisons, the reader is also referred to [81]. It must be pointed out that, under the assumption of small displacement/strain fields, the collapse multiplier is not influenced by the elasticity of the underneath soil. This is why, even for unilateral materials, the limit analysis solution does not depend on foundation displacements as long as they are small, i.e., the set of constraints defining the space of admissible stress states does not change. In contrast, the collapse multiplier and the mechanism would change in large displacements.

5.1. Masonry panel

Geometry, discretisation and loading conditions of the example under analysis are depicted in Fig. 12. Each horizontal layer comprises 6 blocks stacked vertically, defining an interlocked pattern. If the foundation line were fixed, as all the published contributions have supposed so far, the soil response under the traction exerted by the masonry wall would not affect the global mechanical response. Furthermore, any differential settlement could only be prescribed as a known boundary condition and not determined as an unknown of the coupled mechanical problem. The goal of the numerical example is to show the efficiency of the proposed integrated approach. The panel's geometry is defined by $B = 1.2$ m and $H = 3.6$ m with an orthogonal depth $s = 1$ m and self-weight $\gamma = 10$ kN/m^3. The total weight is then $W = 43.2$ kN. The friction angle is assumed as $\mu = 35°$.

The mechanical properties of the soil are modelled assuming a Young moduli $E_{soil} = 500$ MPa. Such a value corresponds to a rather stiff soil (for instance, E of a mixture of sand and gravel is 200 MPa) in order to demonstrate the efficiency of the procedure also for low soil deformability. The iterative procedure considers α and β both equal to 0.1. The horizontal forces are applied incrementally so that, looking at the panel as a single block in unilateral contact with the soil, different positions of the neutral axis can be defined. Two different load combinations are considered as represented in Fig. 12.

A flat, mass-less horizontal block with negligible height is placed on top of the panel to properly apply the above loads. The error tolerances $\text{tol}_{(\cdot)}$ are set equal to 10^{-4} if not indicated differently. The numerical results are obtained by meshing the interface with 108 elements on the half-plane and 18 red elements on the masonry panel. A factor of 500 is used to scale the deformed configurations up. Looking at the results obtained with load condition 1, Section 5.1.1 shows that contact strategy 1 is more efficient than contact strategy 2. Therefore, all the remaining applications are carried out by adopting strategy 1 only. In particular, Section 5.1.2 explores the panel's mechanical response due to load condition 2 considering only contact strategy 1.

5.1.1. Load condition 1

Load condition 1 intends to highlight the differences in behaviour among the classical approach (fixed undeformable foundation) and the two proposed contact strategies (see Section 4.3). For comparison, the panel may also be approximated as a unique rigid block and, hence, the contact pressure between the panel and the soil to be estimated by hand calculations ($3u$ rule). Three levels of horizontal force F_0 are considered, i.e. $F_0 = 0, 5.2, 5.6, 6.0$ kN. The distance d between the corresponding neutral axis and the panel's middle base point would satisfy the *$3u$ rule*, i.e. $d = B/2 - 3 * u$. Consequently, $F_0 = 5.2, 5.6, 6.0$ kN would correspond to $d = 0.10, 0.2, 0.3$ m, respectively. Fig. 13 shows the solutions in terms of deformed configurations obtained by the present approach considering only the self-weight. The solution obtained assuming a rigid, undeformable foundation is not reported as deformed and undeformed are coincident. Fig. 14 compares the deformed configurations using the present approach for different values of F_0. The mechanical response of the panel as a function of the increasing horizontal force F_0 shows an increasing global rotation of the panel together with the deformation of the soil. Fig. 15 shows the normal traction trends on the foundation line, with positive values representing compressive action. Fig. 16 depicts the tangential traction exerted by the masonry on the soil, with positive values indicating direction towards the right. Figs. 15–16 compare the present coupled approach (with both strategies) with the results obtained by modelling the interface as fixed. Moreover, for $F_0 = 0$ kN, the results are also reported by assuming the masonry panel as a unique rigid element in unilateral contact with the interface ($3u$ rule in the legend).

The convergence path associated with strategy 1 converges to the solution within approximately 40–50 iterations versus 100 iterations required by contact strategy 2. In the absence of horizontal force, as illustrated by Fig. 15a, the results show a meaningful stress concentration towards the panel's extreme foundation points, which is expected due to the soil's deformation. Looking at Fig. 15b–d, for $F_0 > 0$ kN, the contact area provided by the present approach is always larger than the one obtained modelling a fixed foundation, which is almost coincident with the one obtained using the $3u$ rule. Interestingly, looking at Fig. 16a in the absence of horizontal load ($F_0 = 0$ kN), the present

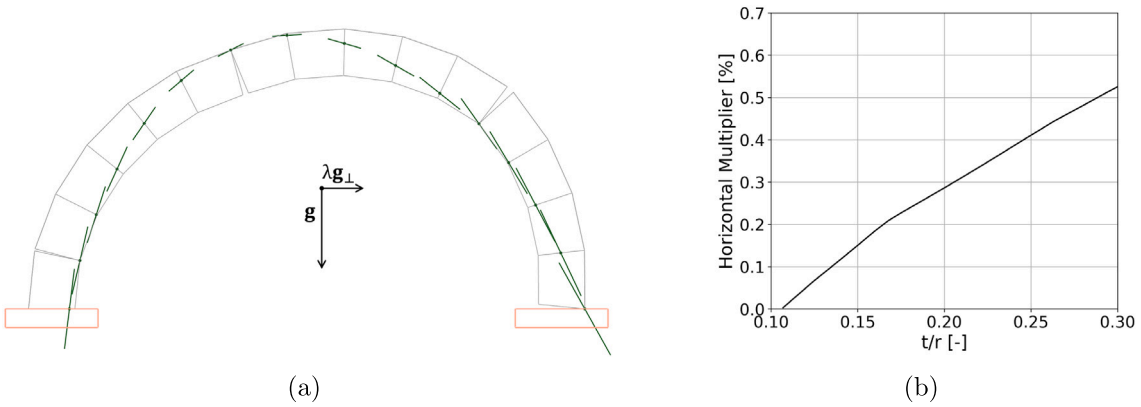

Fig. 11. Collapse mechanism of a semicircular arch subjected to lateral loads (a) and trend of the horizontal multiplier as a function of the thickness t and mean radius r (b).

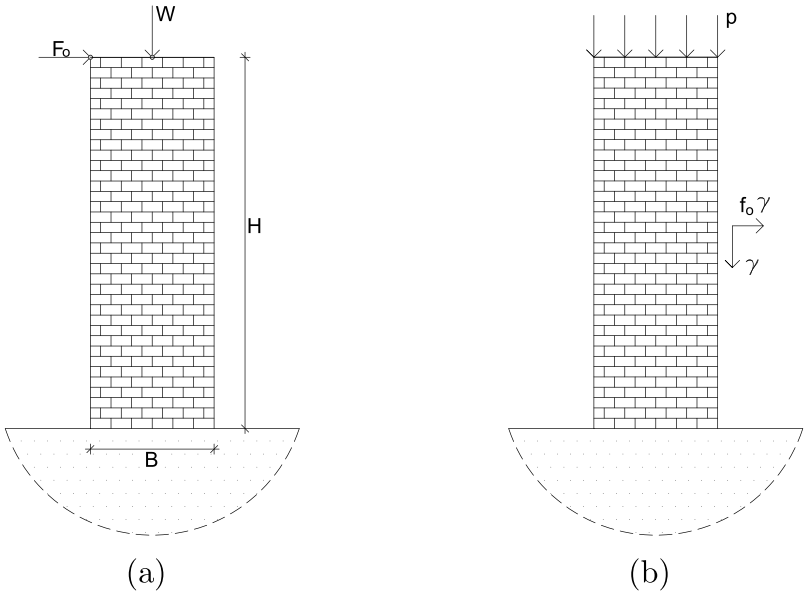

Fig. 12. Loading conditions applied to the masonry panel. (a): Loading condition 1; (b): Loading condition 2.

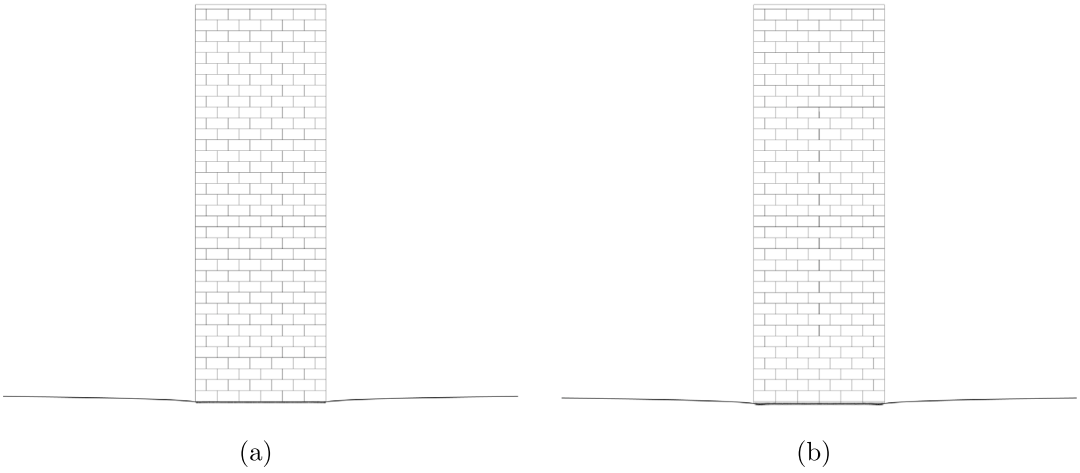

Fig. 13. Panel-soil deformed configurations subjected to load condition 1 and obtained through the proposed coupled approach assuming $F_0 = 0$ kN: (a) contact strategy 1, and (b) contact strategy 2.

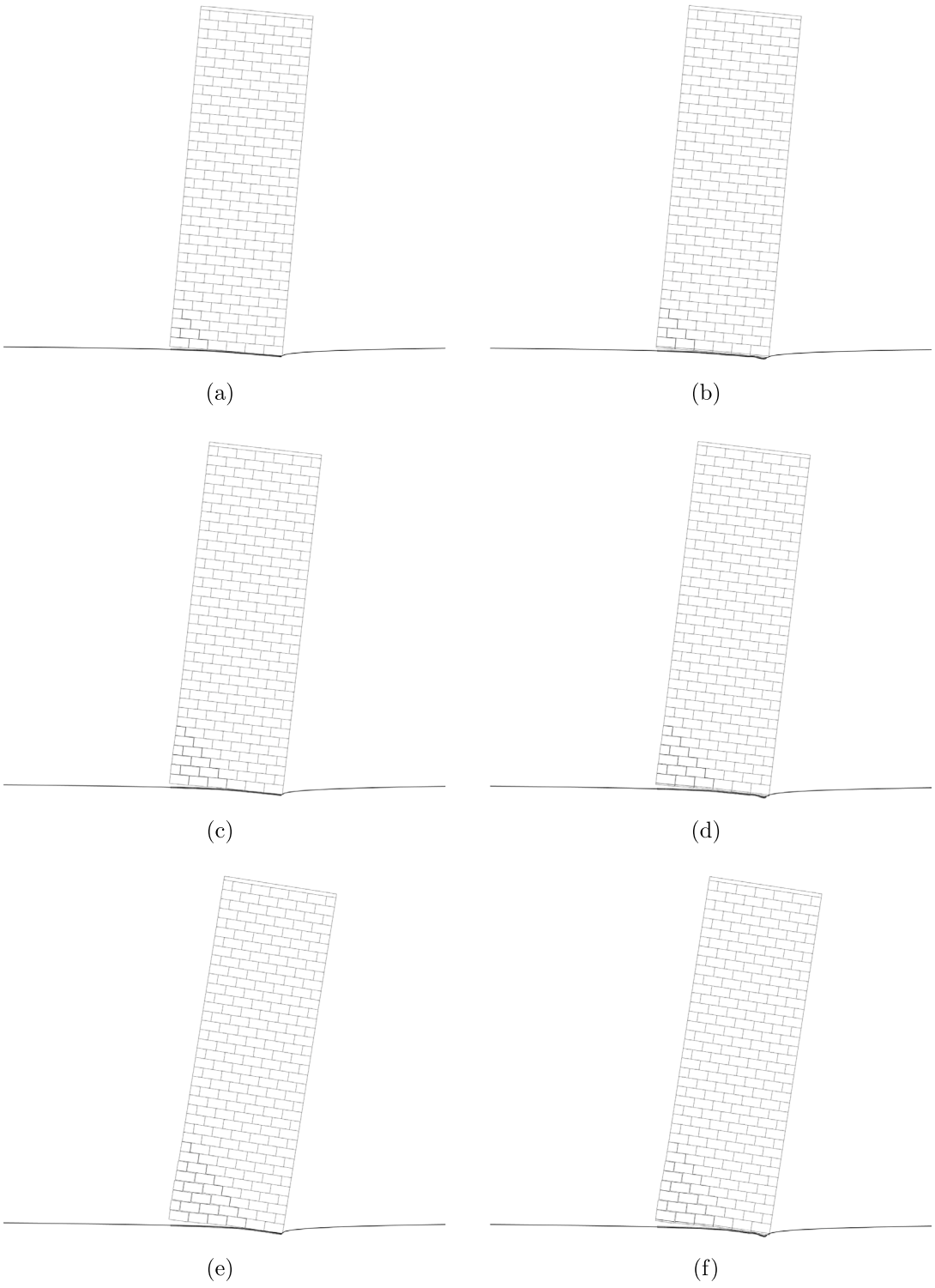

Fig. 14. Deformed configurations of the panel-soil subjected to load condition 1 assuming contact strategy 1 (left) and contact strategy 2 (right). (a–b) $F_0 = 5.2$ kN ($d = 0.10$ m); (c–d) $F_0 = 5.6$ kN ($d = 0.20$ m); (e–f) $F_0 = 6.0$ kN ($d = 0.30$ m).

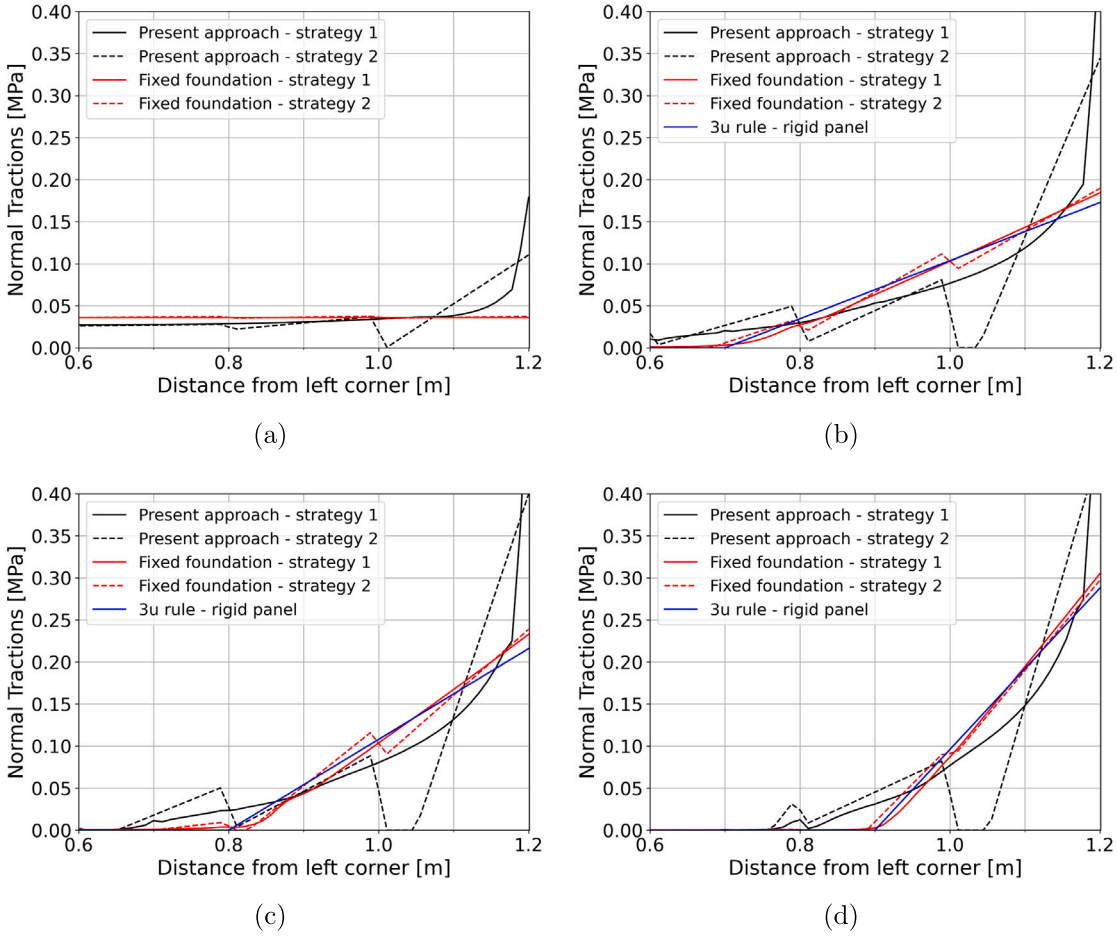

Fig. 15. Normal tractions [MPa] on the foundation line. Loading condition 1. (a) $F_0 = 0.0$ kN, (b) $F_0 = 5.2$ kN ($d = 0.10$ m), (c) $F_0 = 5.6$ kN ($d = 0.20$ m), and (d) $F_0 = 6.0$ kN ($d = 0.30$ m). (For interpretation of the references to colour in this figure legend, the reader is referred to the web version of this article.)

approach shows non-zero symmetric tangential stresses arising between the masonry panel and soil. Contact strategy 1 shows a smoother trend than contact strategy 2, which shows a piece-wise constant behaviour with isolated jumps. In fact, contact strategy 2 models each brick as an independent unit in contact with the soil beneath it, resulting in a linear contact pattern between each brick and the foundation. Consequently, it may allow any brick to be partially in contact with the soil, whereas the adjacent brick achieves full contact, thus introducing a localised jump in the contact tractions. Such a response is rather unrealistic and demonstrates that strategy 1 is more feasible in catching the correct behaviour. For these reasons, subsequent analyses in Sections 5.1.2 and 5.2 will be carried out with contact strategy 1 only.

5.1.2. Loading condition 2

The mechanical problem is solved under the loading condition depicted in Fig. 12b ($p = 10$ kN/m). Four distinct analyses are performed. The first one looks at the panel's response considering only vertical loads. The additional three analyses consider a horizontal volume force multiplier γ. Each block is then subjected to additional horizontal forces proportional to its weight through the scale factor γ. The overall horizontal force is denoted by F_0. Three values of the horizontal multiplier are considered that are $F_0 = 12.78$ kN ($d = 0.05$ m), $F_0 = 13.29$ kN ($d = 0.10$ m), $F_0 = 13.80$ kN ($d = 0.15$ m). Fig. 17 compares the fixed foundation (left column) with the present approach (contact strategy 1 - right column). The normal and tangential traction distributions comparison over the foundation line is shown in Figs. 18–19, respectively.

When $F_0 > 0$, the difference in normal traction and contact area between the present approach and the fixed foundation assumption is less pronounced with respect to the previous load condition. However, the difference in crack patterns and differential settlements is evident as volume forces redirect the internal stress state [81]. Indeed, With increasing F_0, the present approach captures a diagonal crack, but the standard one does not. It explains the typical crack pattern in buttresses subjected to horizontal thrusts exerted by adjacent structures. The order of the crack openings evaluated with the present approach is about 0.1–1 mm. In the case, $F_0 = 13.29$ kN, for instance, the differential settlement is about 0.4 mm, and the ratio between crack openings evaluated with the present approach (i.e. 0.2 mm) is more than one order of magnitude higher than the one with a fixed foundation. The results corresponding to the classical $3u$ rule provide a similar contact zone but with a smoother pressure distribution that underestimates the pressure peak at the corner.

The effect of slenderness is briefly investigated by applying loading condition 2 to a square masonry panel with the same base $B = 1.2$ m. The panel-soil contact line is discretised with the same number (108) of red masonry blocks and the same stiffness contact values. Considering as a reference the rectangular panel depicted in Fig. 17b, subjected to $F_0 = 12.78$ kN ($d = 0.05$ m), which is 78% of its collapse load, two types of comparisons are performed. The first one evaluates the square masonry panel's response when subjected to a horizontal load of $F_0 = 18.33$ kN corresponding to $d = 0.05$ m at the base (see also Section 5.1.1 for an explanation on d). The second comparison tests the square masonry panel under the same percentage (78%) of its collapse load, that is $F_0 = 78\%18.42 = 14.37$ kN where 18.42 kN is its estimated collapse load. The corresponding deformed configurations of the square panel are depicted in Fig. 20a–b, respectively. The diagonal crack in

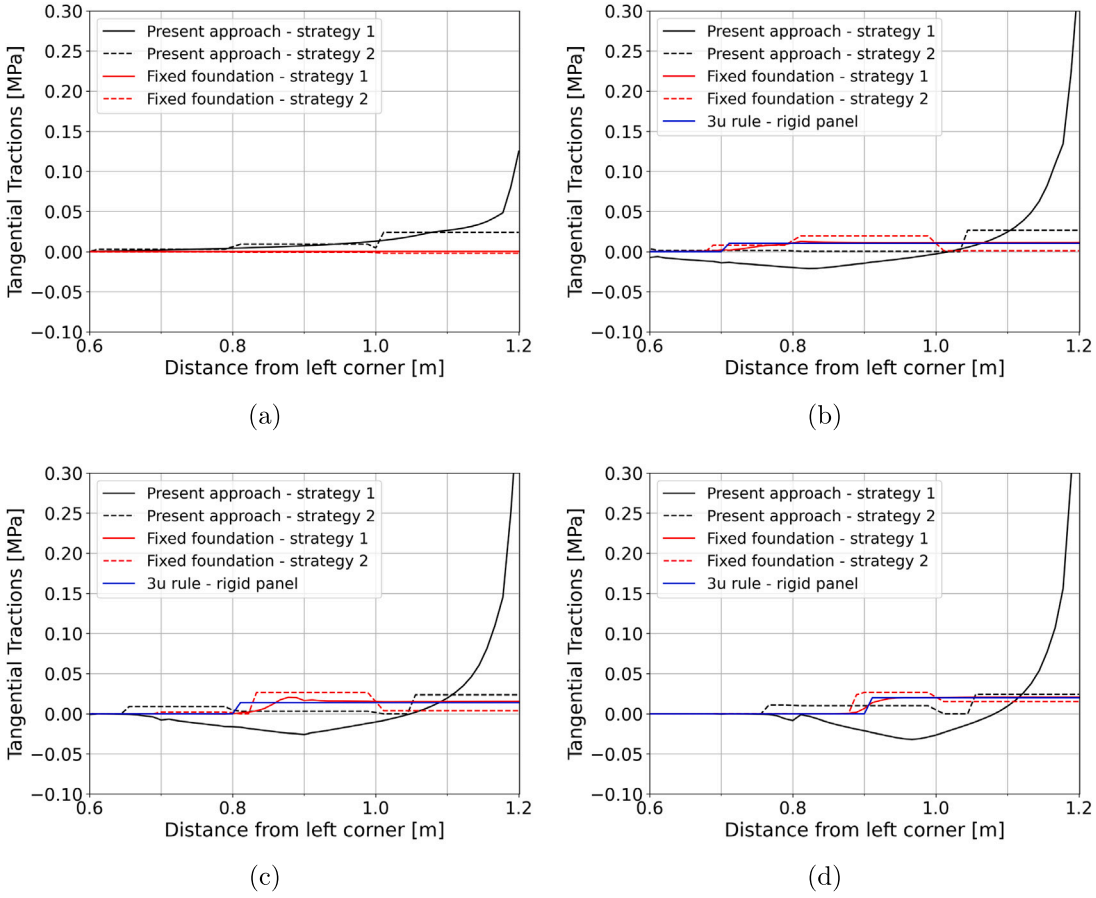

Fig. 16. Tangential tractions [MPa] on the foundation line. Loading condition 1. (a) $F_0 = 0.0$ kN, (b) $F_0 = 5.2$ kN ($d = 0.10$ m), (c) $F_0 = 5.6$ kN ($d = 0.20$ m), and (d) $F_0 = 6.0$ kN ($d = 0.30$ m). (For interpretation of the references to colour in this figure legend, the reader is referred to the web version of this article.)

the square panel is less pronounced with respect to the rectangular plate (compare with Fig. 17b) and almost separates it into two parts. Differently from the rectangular panel, the non-active part of the square panel, defined by the part below the crack, is almost 40%.

5.1.3. Convergence analysis

A convergence analysis has also been conducted to test the sensitivity of the results w.r.t. the number of (red) supporting elements on the interface, i.e. going from 108 to 216 red blocks. In Figs. 21–22 the dashed lines depict the results with 108 blocks, while the continuous lines report the ones obtained by doubling the number of elements. Specifically, Fig. 21a–b refer to the load condition 1 and consider both contact strategies, while Fig. 22a–b illustrate the results using contact strategy 1 only.

As the reader can note, the results do not change while doubling the number of the elements from 108 to 216. Moreover, based on these comparisons, the discretisation adopted in Section 5 is sufficient to obtain reliable results. It is important to note that the consistency of results, as observed here, extends to all cases discussed in the previous section, though not explicitly presented to maintain brevity.

5.2. Masonry arch subjected to a non-symmetrical load

The present section showcases the method's accuracy and reliability on a semicircular masonry arch subjected to a non-symmetrical vertical distributed load. The goal is to show the benefit of including soil deformation in estimating the response of a masonry structure under a simple but meaningful loading condition. Indeed, this loading condition has been selected to highlight the effects of differential settlement on the crack pattern exhibited by the arch. The arch geometry, discredited with 15 voussoirs, is depicted in Fig. 23. It must be pointed out that the arch geometry is not realistic as it is not supported by lateral abutments nor covered by backfill. However, the semicircular arch is a key example studied by many researchers to benchmark new methods, as demonstrated by the rich literature in this sector [10,13,14,38,44,82,83] and references therein. In our case, the arch geometry is selected to highlight how the proposed procedure can capture the pre-collapse hinges, which could not have been modelled using a fixed foundation approach. The arch self-weight is $\gamma = 18$ kN/m^3. The applied load $q = 30$ kN/m is far from the collapse load, which is about 70 kN/m. Twenty supporting elements are placed along the contact interface $\bar{\Gamma}$ between each arch's base and the soil. The arch-soil interaction is studied by considering the soil is made up of clay with or without sand percentages. Three values of the Young modulus are adopted: $E_{soil} = 20$ MPa corresponding to a soft clay, $E_{soil} = 50$ MPa to a mild hard clay and $E_{soil} = 100$ MPa to a hard clay. Opposite to the masonry panel application, the aim was to show the procedure's efficiency with respect to the fixed foundation, even for very stiff soil, where the goal is to show the performance of the proposed approach for real soil.

Fig. 24 illustrates the deformed configurations of the arch scaled up by 50. In the same figure, the straight green lines provide the internal contact forces approximating the thrust line. For obvious reasons, the deformed configuration of the arch subjected to the same load but supported on a rigid foundation is not depicted; indeed, in such a case, the arch does not show any crack patterns, remaining essentially undeformed. The influence of the soil on the response is evident.

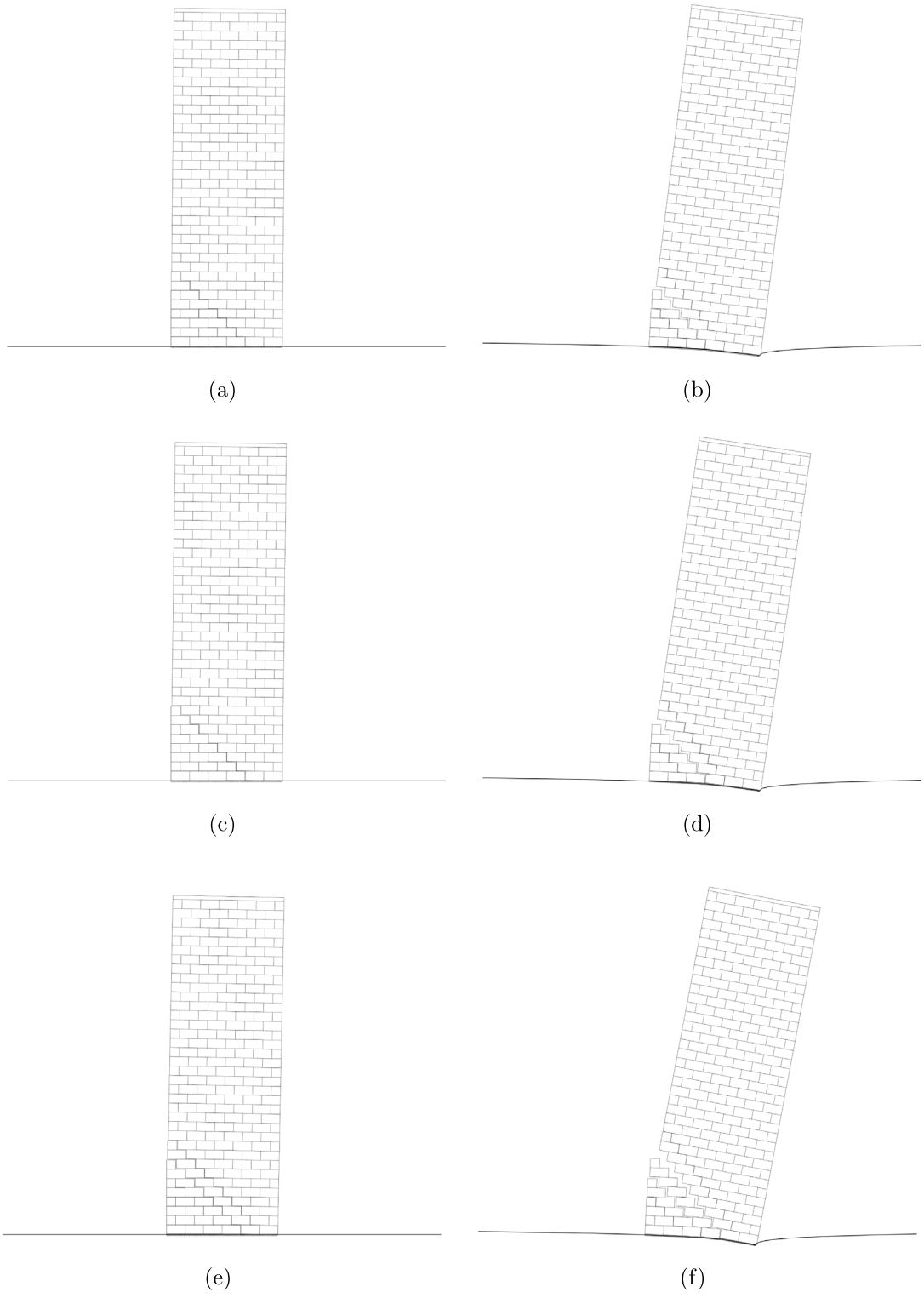

Fig. 17. Deformed configurations of the panel subjected to load condition 2 with fixed foundation (left) and the present approach with contact strategy 1 (right). (a–b) $F_0 = 12.78$ kN ($d = 0.05$ m); (c–d) $F_0 = 13.29$ kN ($d = 0.10$ m); (e–f) $F_0 = 13.80$ kN ($d = 0.15$ m).

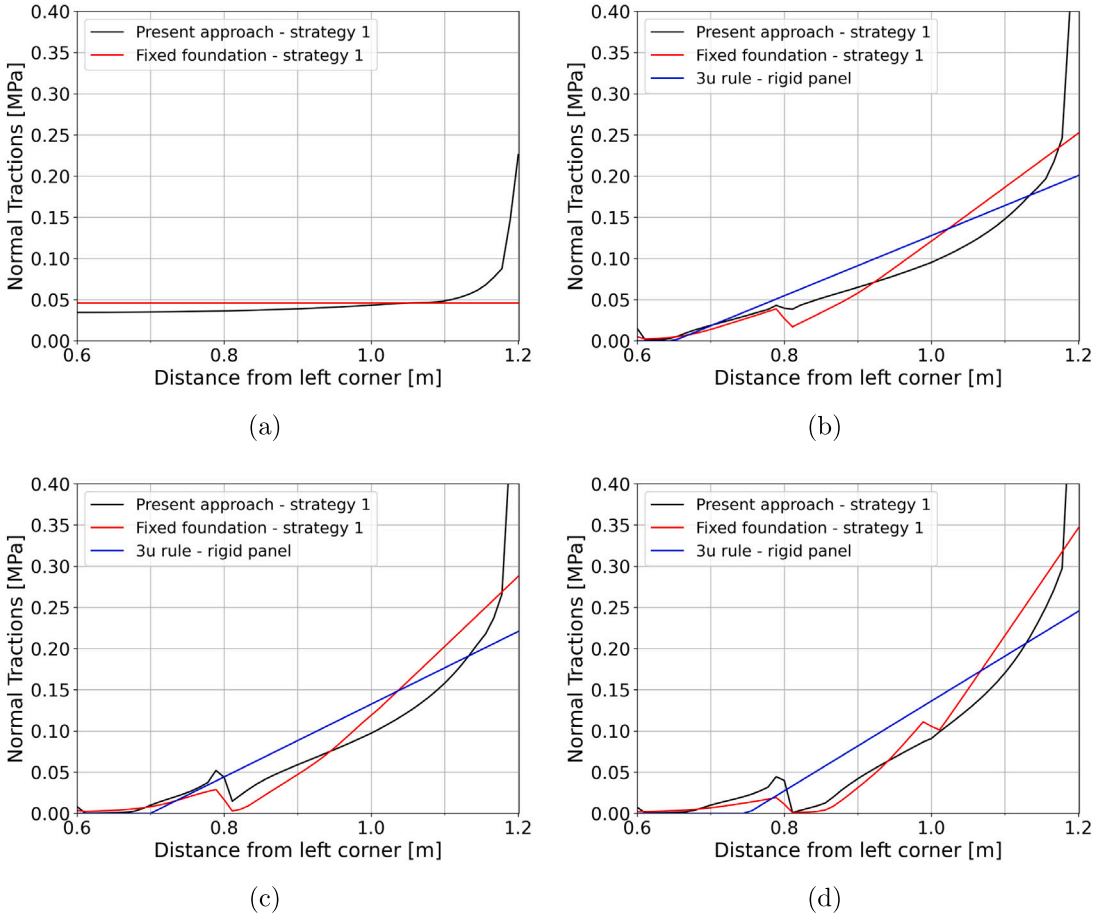

Fig. 18. Normal tractions [MPa] on the foundation line due to the loading condition 2. (a) $F_0 = 0.0$ kN, (b) $F_0 = 12.78$ kN ($d = 0.05$ m), (c) $F_0 = 13.29$ kN ($d = 0.10$ m) and (d) $F_0 = 13.8$ kN ($d = 0.15$ m). (For interpretation of the references to colour in this figure legend, the reader is referred to the web version of this article.)

Indeed, as the reader can note, by reducing the value of E_{soil}, the soil's deformed configuration, and hence the crack opening amplifies. It is worth recalling that a collapse mechanism, in the case of non-symmetric load, is defined by a four-hinge mechanism. In all cases, the semicircular arch shows two hinges, while two additional ones are needed to bring the arch to the collapse.

By decreasing the half-plane stiffness from $E = 100$ MPa (Fig. 24a) to $E = 20$ MPa (Fig. 24c), the effects of soil on the global response are even more evident, being the size of the crack openings higher. Indeed, the maximum width of the hinge goes from about 0.9 mm for $E_{soil} = 100$ MPa to about 5 mm when $E_{soil} = 20$ MPa. The internal force distribution is compliant with the corresponding crack pattern. It must be underlined that such a crack pattern would not occur if the model included the foundation as rigid.

6. Summary and conclusions

The present research proposes a new approach to model differential settlements beneath masonry foundations and the corresponding induced crack patterns. It directly considers the influence of soil on the structural response. Based on the no-tension assumption, the masonry domain is discretised into a finite number of elastic bodies in unilateral, Mohr–Coulomb-associated friction contact, with the elasticity of the blocks lumped at the interfaces between them. The corresponding boundary value problem is solved using the minimum of the complementary energy and framed as an optimisation problem.

The soil is modelled as an elastic half-plane using the appropriate fundamental solutions of the Melan problem, allowing the discretisation of only the masonry-soil contact areas. Compatibility is imposed at the masonry-soil interface by properly modelling the non-linear contact, while equilibrium conditions are enforced by adopting two alternative contact strategies. An iterative procedure is set up to solve the coupled problem, ensuring that the solution simultaneously satisfies both equilibrium and displacement compatibility constraints.

The two contact strategies were fully explored numerically on a masonry panel under several loading scenarios. As the main outcome, the first contact strategy (Section 4.3.1) provided more appropriate results with faster convergence. Furthermore, the method's potential was demonstrated in a practical engineering application involving a masonry arch under non-symmetric loading conditions, fully capturing the effect of soil deformation on the mechanical response of the masonry.

From an engineering perspective, the proposed coupled approach offers new potential to describe complex foundation settlements and crack patterns, particularly when the load is far from the structure's maximum capacity. In such cases, it allows for the description of crack patterns that other approaches can only capture by considering a priori-prescribed foundation displacements. Looking at the masonry panel, it was shown that the crack size revealed by the proposed coupled approach is at least one order of magnitude larger than that captured by considering only the elastic compressive response of the masonry. Additionally, the proposed approach, as shown in Section 5.1.2, provides an explanation for typical diagonal crack patterns exhibited by buttresses. This aspect, emphasised by the arch analysis, demonstrates

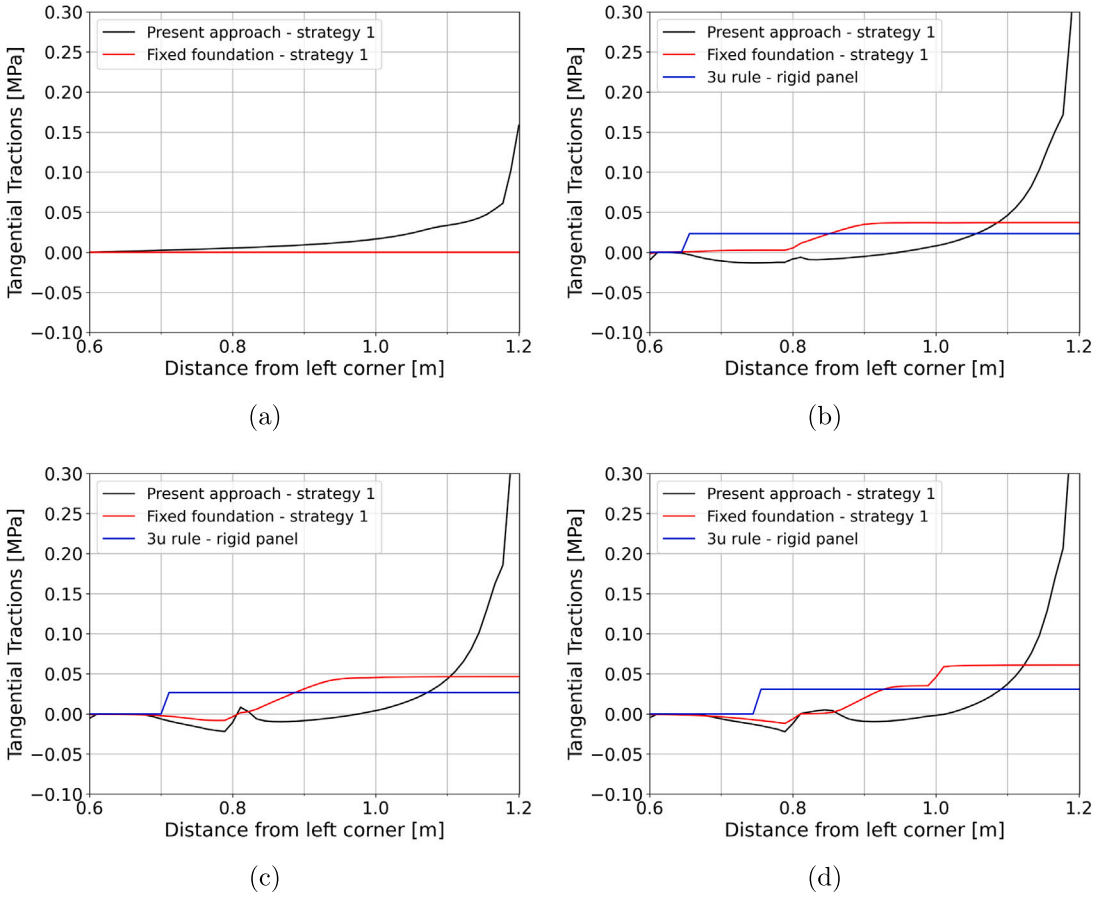

Fig. 19. Tangential tractions [MPa] on the foundation line due to the loading condition 2. (a) $F_0 = 0.0$ kN, (b) $F_0 = 12.78$ kN ($d = 0.05$ m), (c) $F_0 = 13.29$ kN ($d = 0.10$ m) and (d) $F_0 = 13.80$ kN ($d = 0.15$ m). (For interpretation of the references to colour in this figure legend, the reader is referred to the web version of this article.)

Fig. 20. Solution of the soil–structure contact problem involving a square masonry panel subjected to load condition 2 and assuming contact strategy 1: deformed configuration due to $F_0 = 18.33$ kN ($d = 0.05$) (a) and $F_0 = 14.37$ kN = 78% of its collapse load (b).

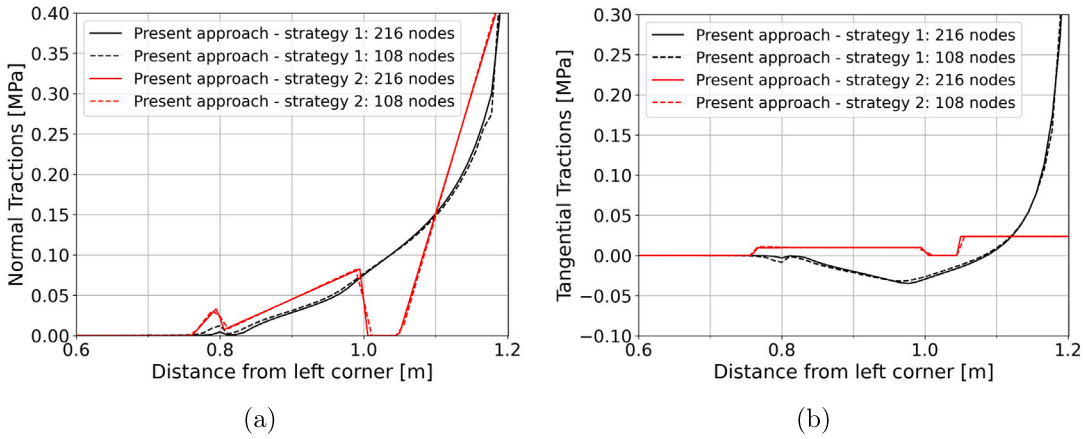

Fig. 21. Convergence analysis related to load condition 1 ($F_0 = 6.0$ kN - $d = 0.3$ m): normal (a) and tangential (b) tractions [MPa] exerted by the masonry panel on the foundation line discretised with 108 and 216 supporting (red) elements. (For interpretation of the references to colour in this figure legend, the reader is referred to the web version of this article.)

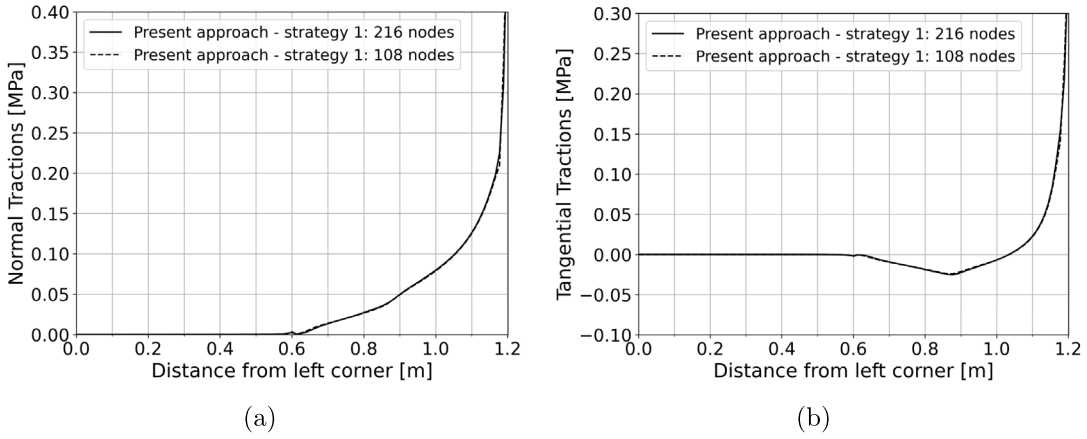

Fig. 22. Convergence analysis related to load condition 2 ($F_0 = 13.80$ kN - $d = 0.15$ m): normal (a) and tangential (b) tractions [MPa] exerted by the masonry panel on the foundation line discretised with 108 and 216 supporting (red) elements.

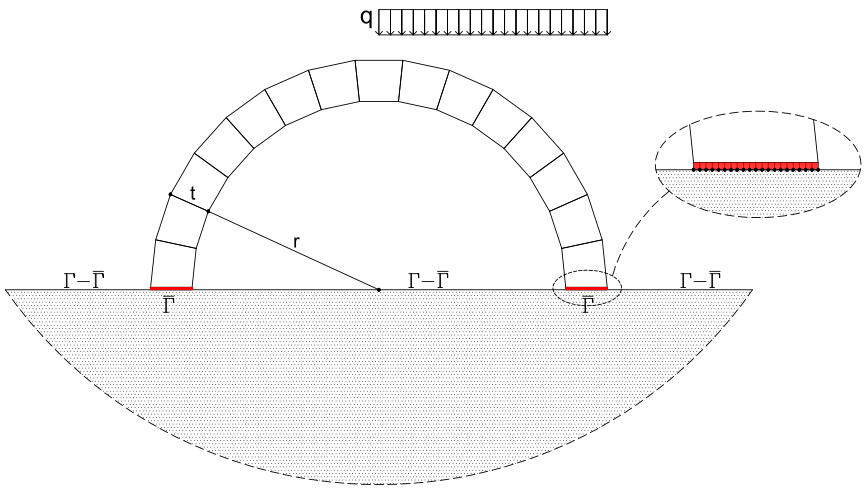

Fig. 23. The semicircular arch geometry is defined by $r = 2.7$ m, $t = 0.6$ m, while the non-symmetric uniformly distributed load is $q = 30$ kN/m.

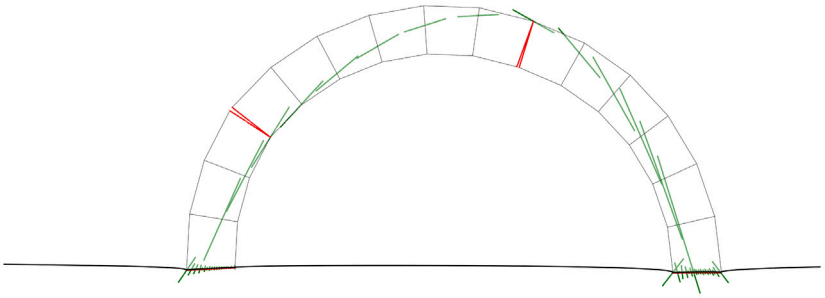

(a)

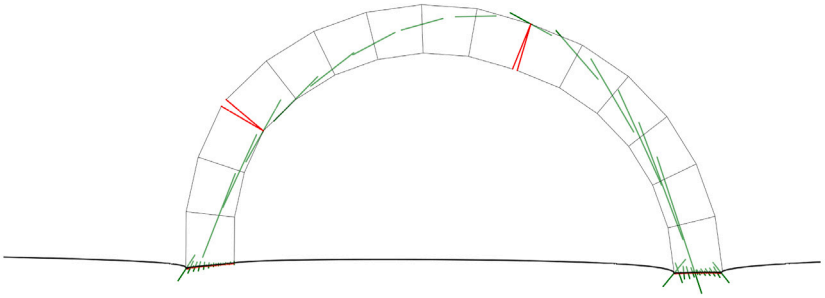

(b)

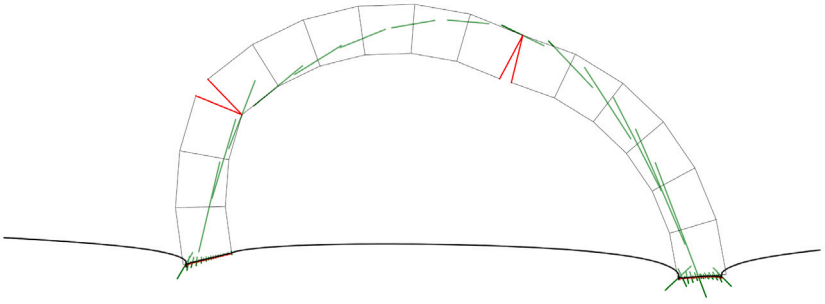

(c)

Fig. 24. Arch deformed configuration and internal contact forces for three different values of Young's moduli of the soil: E_{soil} = 100 MPa (a), 50 MPa (b), 20 MPa (c). Hinges are highlighted by red lines. (For interpretation of the references to colour in this figure legend, the reader is referred to the web version of this article.)

the ability to capture phenomena in terms of crack patterns under safe load conditions that standard approaches cannot.

CRediT authorship contribution statement

Antonino Iannuzzo: Writing – review & editing, Validation, Software, Methodology, Data curation. **Vincenzo Mallardo:** Writing – review & editing, Writing – original draft, Validation, Supervision, Software, Methodology, Conceptualization.

Declaration of competing interest

The authors declare the following financial interests/personal relationships which may be considered as potential competing interests: Antonino Iannuzzo reports financial support was provided by Italian Ministry of University and Research. If there are other authors, they declare that they have no known competing financial interests or personal relationships that could have appeared to influence the work reported in this paper.

Acknowledgements

The research was funded by the Italian Ministry of University and Research through the Programme "Rita Levi Montalcini for young researchers" (FFO 2020 - Funding ID: DM0001039.25-08-2022).

Data availability

Data will be made available on request.

References

[1] Angelillo M. Constitutive relations for no-tension materials. Meccanica 1993;28:195–202. http://dx.doi.org/10.1007/BF00989121.
[2] Del Piero G. Limit analysis and no-tension materials. Int J Plast 1998;14(1–3):259–71. http://dx.doi.org/10.1016/S0749-6419(97)00055-7.
[3] Alfano G, Rosati L, Valoroso N. A numerical strategy for finite element analysis of no-tension materials. Int J Numer Methods Eng 2000;48(3):317–50. http://dx.doi.org/10.1002/(SICI)1097-0207(20000530)48:3<317::AID-NME868>3.0.CO;2-C.
[4] Zucchini A, Lourenço PB. A micro-mechanical homogenisation model for masonry: Application to shear walls. Int J Solids Struct 2009;46(3–4):871–86. http://dx.doi.org/10.1016/j.ijsolstr.2008.09.034.
[5] Angelillo M, Cardamone L, Fortunato A. A numerical model for masonry-like structures. J Mech Mater Struct 2010;5(4):583–615. http://dx.doi.org/10.2140/jomms.2010.5.583.
[6] Bagi K. When Heyman's Safe Theorem of rigid block systems fails: Non-Heymanian collapse modes of masonry structures. Int J Solids Struct 2014;51(14):2696–705. http://dx.doi.org/10.1016/j.ijsolstr.2014.03.041.
[7] Addessi D, Sacco E. Nonlinear analysis of masonry panels using a kinematic enriched plane state formulation. Int J Solids Struct 2016;90:194–214. http://dx.doi.org/10.1016/j.ijsolstr.2016.03.002.
[8] Baraldi D, Cecchi A. A full 3D rigid block model for the collapse behaviour of masonry walls. Eur J Mech A Solids 2017;64:11–28. http://dx.doi.org/10.1016/j.euromechsol.2017.01.012.
[9] Zampieri P, Zanini MA, Faleschini F, Hofer L, Pellegrino C. Failure analysis of masonry arch bridges subject to local pier scour. Eng Fail Anal 2017;79:371–84. http://dx.doi.org/10.1016/j.engfailanal.2017.05.028.
[10] Galassi S, Misseri G, Rovero L, Tempesta G. Failure modes prediction of masonry voussoir arches on moving supports. Eng Struct 2018;173:706–17. http://dx.doi.org/10.1016/j.engstruct.2018.07.015.
[11] Addessi D, Di Re P, Sacco E. Micromechanical and multiscale computational modeling for stability analysis of masonry elements. Eng Struct 2020;211:110428. http://dx.doi.org/10.1016/j.engstruct.2020.110428.
[12] Li Y, Zeng B. Modeling of masonry structures using a new 3D cohesive interface material model considering dilatancy softening. Eng Struct 2023;277:115466. http://dx.doi.org/10.1016/j.engstruct.2022.115466.
[13] Galassi S, Zampieri P. A new automatic procedure for nonlinear analysis of masonry arches subjected to large support movements. Eng Struct 2023;276:115359. http://dx.doi.org/10.1016/j.engstruct.2022.115359.
[14] Galassi S. An alternative approach for limit analysis of masonry arches on moving supports in finite small displacements. Eng Fail Anal 2023;145:107004. http://dx.doi.org/10.1016/j.engfailanal.2022.107004.
[15] D'Altri A, Sarhosis V, Milani G, Rots J, Cattari S, Lagomarsino S, Sacco E, Tralli A, Castellazzi G, De Miranda S. A review of numerical models for masonry structures. Elsevier; 2019, p. 3–53. http://dx.doi.org/10.1016/B978-0-08-102439-3.00001-4.
[16] Milani G, Lourenço P, Tralli A. 3D homogenized limit analysis of masonry buildings under horizontal loads. Eng Struct 2007;29(11):3134–48. http://dx.doi.org/10.1016/j.engstruct.2007.03.003.
[17] Milani G, Cecchi A. Compatible model for herringbone bond masonry: Linear elastic homogenization, failure surfaces and structural implementation. Int J Solids Struct 2013;50(20–21):3274–96. http://dx.doi.org/10.1016/j.ijsolstr.2013.05.032.
[18] Scacco J, Grillanda N, Milani G, Lourenço PB. Novel non-linear static numerical model for curved masonry structures based on a combined adaptive limit analysis and discrete FE computations. Int J Solids Struct 2022;236:111265. http://dx.doi.org/10.1016/j.ijsolstr.2021.111265.
[19] Gobbin F, de Felice G, Lemos JV. Numerical procedures for the analysis of collapse mechanisms of masonry structures using discrete element modelling. Eng Struct 2021;246:113047. http://dx.doi.org/10.1016/j.engstruct.2021.113047.
[20] de Oliveira Neto L, Masia MJ, Almeida V, Simonetti HL. A nonlinear BE formulation for analysis of masonry walls considering orthotropy: Fundamentals. Structures 2021;33:3944–53. http://dx.doi.org/10.1016/j.istruc.2021.06.103.
[21] Mallardo V. Integral equations and nonlocal damage theory: a numerical implementation using the BDEM. Int J Fract 2009;157:13–32. http://dx.doi.org/10.1007/s10704-008-9297-0.
[22] Munjiza A. The combined finite-discrete element method. John Wiley & Sons; 2004, http://dx.doi.org/10.1002/0470020180.
[23] Smoljanović H, Nikolić Z, Živaljić N. A combined finite-discrete numerical model for analysis of masonry structures. Eng Fract Mech 2015;136:1–14. http://dx.doi.org/10.1016/j.engfracmech.2015.02.006.
[24] Baraldi D, Reccia E, Cecchi A. In plane loaded masonry walls: DEM and FEM/DEM models. A critical review. Meccanica 2018;53:1613–28. http://dx.doi.org/10.1007/s11012-017-0704-3.
[25] Reccia E, Cazzani A, Cecchi A. FEM-DEM modeling of out-of-plane loaded masonry panels: A limit analysis approach. Open Civ Eng J 2012;6:231–8. http://dx.doi.org/10.2174/1874149501206010231.
[26] Heyman J. The stone skeleton. Int J Solids Struct 1966;2(2):249–79. http://dx.doi.org/10.1016/0020-7683(66)90018-7.
[27] Stavroulakis G. On the static behaviour of cracked masonry walls. Eur J Mech A Solids 1990;9(4):341–58.
[28] Cuomo M, Ventura G. A complementary energy formulation of no tension masonry-like solids. Comput Methods Appl Mech Engrg 2000;189(1):313–39. http://dx.doi.org/10.1016/S0045-7825(99)00298-4.
[29] Iannuzzo A, Van Mele T, Block P. Piecewise rigid displacement (PRD) method: A limit analysis-based approach to detect mechanisms and internal forces through two dual energy criteria. Mech Res Commun 2020;107:103557. http://dx.doi.org/10.1016/j.mechrescom.2020.103557.
[30] Block P, Ochsendorf J. Thrust network analysis: a new methodology for three-dimensional equilibrium. J Int Assoc Shell Spatial Struct 2007;48(3):167–73.
[31] Marmo F, Rosati L. Reformulation and extension of the thrust network analysis. Comput Struct 2017;182:104–18. http://dx.doi.org/10.1016/j.compstruc.2016.11.016.
[32] Fraddosio A, Lepore N, Piccioni MD. Thrust surface method: An innovative approach for the three-dimensional lower bound limit analysis of masonry vaults. Eng Struct 2020;202:109846. http://dx.doi.org/10.1016/j.engstruct.2019.109846.
[33] Bigoni D, Noselli G. Localized stress percolation through dry masonry walls. Part I–experiments. Eur J Mech A Solids 2010;29(3):291–8. http://dx.doi.org/10.1016/j.euromechsol.2009.10.009.
[34] Bigoni D, Noselli G. Localized stress percolation through dry masonry walls. Part II–modelling. Eur J Mech A Solids 2010;29(3):299–307. http://dx.doi.org/10.1016/j.euromechsol.2009.10.013.
[35] Chen S, Bagi K. Crosswise tensile resistance of masonry patterns due to contact friction. Proc R Soc A 2020;476(2240):20200439. http://dx.doi.org/10.1098/rspa.2020.0439.
[36] Casapulla C, Mousavian E, Argiento L, Ceraldi C, Bagi K. Torsion-shear behaviour at the interfaces of rigid interlocking blocks in masonry assemblages: experimental investigation and analytical approaches. Mater Struct 2021;54(3):134. http://dx.doi.org/10.1617/s11527-021-01721-x.
[37] Giardina G, Marini A, Hendriks MA, Rots JG, Rizzardini F, Giuriani E. Experimental analysis of a masonry façade subject to tunnelling-induced settlement. Eng Struct 2012;45:421–34. http://dx.doi.org/10.1016/j.engstruct.2012.06.042.
[38] Galassi S, Misseri G, Rovero L. Capacity assessment of masonry arches on moving supports in large displacements: Numerical model and experimental validation. Eng Fail Anal 2021;129:105700. http://dx.doi.org/10.1016/j.engfailanal.2021.105700.
[39] Ferrero C, Calderini C, Roca P. Experimental response of a scaled dry-joint masonry arch subject to inclined support displacements. Eng Struct 2022;253:113804. http://dx.doi.org/10.1016/j.engstruct.2021.113804.
[40] Iannuzzo A, Angelillo M, De Chiara E, De Guglielmo F, De Serio F, Ribera F, Gesualdo A. Modelling the cracks produced by settlements in masonry structures. Meccanica 2018;53:1857–73. http://dx.doi.org/10.1007/s11012-017-0721-2.

[41] Tralli A, Chiozzi A, Grillanda N, Milani G. Masonry structures in the presence of foundation settlements and unilateral contact problems. Int J Solids Struct 2020;191:187–201. http://dx.doi.org/10.1016/j.ijsolstr.2019.12.005.
[42] Iannuzzo A, Block P, Angelillo M, Gesualdo A. A continuous energy-based numerical approach to predict fracture mechanisms in masonry structures: CDF method. Comput Struct 2021;257:106645. http://dx.doi.org/10.1016/j.compstruc.2021.106645.
[43] Montanino A, De Gregorio D, Olivieri C, Iannuzzo A. The continuous airy-based for stress-singularities (CASS) method: An energy-based numerical formulation for unilateral materials. Int J Solids Struct 2022;256:111954. http://dx.doi.org/10.1016/j.ijsolstr.2022.111954.
[44] Coccia S, Di Carlo F, Rinaldi Z. Collapse displacements for a mechanism of spreading-induced supports in a masonry arch. Int J Adv Struct Eng (IJASE) 2015;7:307–20. http://dx.doi.org/10.1007/s40091-015-0101-x.
[45] Ochsendorf J. Masonry arch on spreading supports. Struct Eng 2006;84(2):29–34.
[46] Portioli F, Cascini L. Assessment of masonry structures subjected to foundation settlements using rigid block limit analysis. Eng Struct 2016;113:347–61. http://dx.doi.org/10.1016/j.engstruct.2016.02.002.
[47] Portioli F, Cascini L. Large displacement analysis of dry-jointed masonry structures subjected to settlements using rigid block modelling. Eng Struct 2017;148:485–96. http://dx.doi.org/10.1016/j.engstruct.2017.06.073.
[48] Tiberti S, Grillanda N, Mallardo V, Milani G. A genetic algorithm adaptive homogeneous approach for evaluating settlement-induced cracks in masonry walls. Eng Struct 2020;221:111073. http://dx.doi.org/10.1016/j.engstruct.2020.111073.
[49] Gagliardo R, Portioli F, Cascini L, Landolfo R, Lourenço PB. A rigid block model with no-tension elastic contacts for displacement-based assessment of historic masonry structures subjected to settlements. Eng Struct 2021;229:111609. http://dx.doi.org/10.1016/j.engstruct.2020.111609.
[50] Portioli F, Cascini L, Landolfo R, Lourenço PB. An optimization-based rigid block modeling approach to seismic assessment of dry-joint masonry structures subjected to settlements. Soil Dyn Earthq Eng 2023;166:107760. http://dx.doi.org/10.1016/j.soildyn.2023.107760.
[51] Giardina G, Van de Graaf AV, Hendriks MA, Rots JG, Marini A. Numerical analysis of a masonry façade subject to tunnelling-induced settlements. Eng Struct 2013;54:234–47. http://dx.doi.org/10.1016/j.engstruct.2013.03.055.
[52] Alessandri C, Garutti M, Mallardo V, Milani G. Crack patterns induced by foundation settlements: integrated analysis on a renaissance masonry palace in Italy. Int J Archit Herit 2015;9(2):111–29. http://dx.doi.org/10.1080/15583058.2014.951795.
[53] Ferrero C, Calderini C, Portioli F, Roca P. Large displacement analysis of dry-joint masonry arches subject to inclined support movements. Eng Struct 2021;238:112244. http://dx.doi.org/10.1016/j.engstruct.2021.112244.
[54] Chen X, Wang X, Wang H, Agrawal AK, Chan AH, Cheng Y. Simulating the failure of masonry walls subjected to support settlement with the combined finite-discrete element method. J Build Eng 2021;43:102558. http://dx.doi.org/10.1016/j.jobe.2021.102558.
[55] Pepe M, Sangirardi M, Reccia E, Pingaro M, Trovalusci P, de Felice G. Discrete and continuous approaches for the failure analysis of masonry structures subjected to settlements. Front Built Environ 2020;6:43. http://dx.doi.org/10.3389/fbuil.2020.00043.
[56] Prosperi A, Longo M, Korswagen PA, Korff M, Rots JG. Sensitivity modelling with objective damage assessment of unreinforced masonry façades undergoing different subsidence settlement patterns. Eng Struct 2023;286:116113. http://dx.doi.org/10.1016/j.engstruct.2023.116113.
[57] Telles J, Brebbia C. Boundary element solution for half-plane problems. Int J Solids Struct 1981;17(12):1149–58. http://dx.doi.org/10.1016/0020-7683(81)90094-9.
[58] Del Piero G. Constitutive equation and compatibility of the external loads for linear elastic masonry-like materials. Meccanica 1989;24:150–62. http://dx.doi.org/10.1007/BF01559418.
[59] Giaquinta M, Giusti E. Researches on the equilibrium of masonry structures. Arch Ration Mech Anal 1985;88:359–92. http://dx.doi.org/10.1007/BF00250872.
[60] Angelillo M, Rosso F. On statically admissible stress fields for a plane masonry-like structure. Quart Appl Math 1995;731–51. http://dx.doi.org/10.1090/qam/1359508.
[61] Lucchesi M, Padovani C, Zani N. Masonry-like solids with bounded compressive strength. Int J Solids Struct 1996;33(14):1961–94. http://dx.doi.org/10.1016/0020-7683(95)00143-3.
[62] Lucchesi M, Silhavy M, Zani N. Singular equilibrated stress fields for no-tension panels. In: Mechanical modelling and computational issues in civil engineering. Springer; 2005, p. 255–65. http://dx.doi.org/10.1007/3-540-32399-6-12.
[63] Lucchesi M, Padovani C, Pasquinelli G, Zani N. Masonry constructions: Mechanical models and numerical applications. Springer Science & Business Media; 2008, http://dx.doi.org/10.1007/978-3-540-79111-9.
[64] Olivieri C, Iannuzzo A, Fortunato A, DeJong MJ. The effect of concentrated loads on open-well masonry spiral stairs. Eng Struct 2022;272:114952. http://dx.doi.org/10.1016/j.engstruct.2022.114952.
[65] Panagiotopoulos PD. Inequality problems in mechanics and applications: Convex and nonconvex energy functions. Springer Science & Business Media; 2012, http://dx.doi.org/10.1007/978-1-4612-5152-1.
[66] Šilhavỳ M. Mathematics of the masonry–like model and limit analysis. In: Mechanics of masonry structures. Springer; 2014, p. 29–69. http://dx.doi.org/10.1007/978-3-7091-1774-3-2.
[67] Angelillo M, Fortunato A, Montanino A, Lippiello M. Singular stress fields in masonry structures: Derand was right. Meccanica 2014;49:1243–62. http://dx.doi.org/10.1007/s11012-014-9880-6.
[68] Ambrosio L, Fusco N, Pallara D. Functions of bounded variation and free discontinuity problems. Oxford University Press; 2000, http://dx.doi.org/10.1093/oso/9780198502456.001.0001.
[69] McInerney J, DeJong M. Discrete element modeling of groin vault displacement capacity. Int J Archit Herit 2015;9(8):1037–49. http://dx.doi.org/10.1080/15583058.2014.923953.
[70] Sarhosis V, Bagi K, Lemos JV, Milani G. Computational modeling of masonry structures using the discrete element method. IGI Global; 2016, http://dx.doi.org/10.4018/978-1-5225-0231-9.
[71] Melan E. Der spannungszustand der durch eine einzelkraft in innern beanspruchten halbscheibe. Z Angew Math Mech 1932;12:343–6.
[72] Johnson KL. Contact mechanics. Cambridge University Press; 1985.
[73] Timoshenko S, Goodier JN. Theory of elasticity. 3rd ed.. McGraw-Hill; 1970.
[74] Brebbia CA, Telles JCF, Wrobel LC. Boundary element techniques: Theory and applications in engineering. Springer Science & Business Media; 2012.
[75] Aliabadi MH. The boundary element method, volume 2: Applications in solids and structures, vol. 2, John Wiley & Sons; 2002.
[76] Poulos HG, Davis EH. Elastic solutions for soil and rock mechanics. Wiley; 1973.
[77] Zampieri P, Faleschini F, Zanini MA, Simoncello N. Collapse mechanisms of masonry arches with settled springing. Eng Struct 2018;156:363–74. http://dx.doi.org/10.1016/j.engstruct.2017.11.048.
[78] Alessandri C, Mallardo V. Crack identification in two-dimensional unilateral contact mechanics with the boundary element method. Comput Mech 1999;24(2):100–9. http://dx.doi.org/10.1007/s004660050442.
[79] Elleithy WM, Tanaka M. Interface relaxation algorithms for BEM–BEM coupling and FEM–BEM coupling. Comput Methods Appl Mech Engrg 2003;192(26–27):2977–92. http://dx.doi.org/10.1016/S0045-7825(03)00312-8.
[80] Mosek A. The MOSEK optimization software. 2010;54(2–1):5. Online at http://www.mosek.com.
[81] Iannuzzo A, Montanino A. A limit analysis-based CASS approach for the in-plane seismic capacity of masonry façades. Int J Solids Struct 2024;289:112633. http://dx.doi.org/10.1016/j.ijsolstr.2023.112633.
[82] Alexakis H, Makris N. Limit equilibrium analysis and the minimum thickness of circular masonry arches to withstand lateral inertial loading. Arch Appl Mech 2014;84:757–72. http://dx.doi.org/10.1007/s00419-014-0831-4.
[83] Varró R, Bögöly G, Görög P. Laboratory and numerical analysis of failure of stone masonry arches with and without reinforcement. Eng Fail Anal 2021;123:105272. http://dx.doi.org/10.1016/j.engfailanal.2021.105272.